17

Detection of Oxidative Stress Biomarkers Using Novel Nanostructured Biosensors

Maria Hepel and Magdalena Stobiecka
State University of New York at Potsdam, Potsdam, NY 13676
USA

1. Introduction

The oxidative stress is associated with the diminished capacity of a biological system to counteract an overproduction or invasion of reactive oxygen species and other radicals. Since oxidative stress is the leading cause of DNA damage, genetic disorders, cancer, and many environmental pollution related diseases, there is an urging need for oxidative stress screening and its prevention. There is growing evidence that oxidative stress may cause autism in children. The oxidative stress has also been implicated in the development of diabetes. Several biomarkers of oxidative stress have been identified, including glutathione (GSH), 3-nitrotyrosine (NT), homocysteine (Hcys), and cysteine (Cys). The tripeptide glutathione and its oxidized form, glutathione disulphide (GSSG), form a redox potential maintenance system in all eukaryotic cells. Since glutathione efficiently protects the DNA, proteins and lipid membranes from radical attacks, its diminished level is signaling an oxidative stress and the increased vulnerability of a biological entity to the environmental influences. An increased level of 3-nitrotyrosine, which is formed under oxidative stress in the presence of nitric oxide, has been found in diabetic patients. Homocysteine is a biomarker and an active agent leading to cardiovascular deterioration. While these biomarkers can be accurately determined using advanced instrumental assays, a wide screening would require the development of small, inexpensive, rapid, and simple in operation platforms for biomarker analysis. In this Chapter, the detection methods for the oxidative stress biomarkers based on their interactions with monolayer-protected gold nanoparticles (AuNP) are described. The nanoparticle utilization in a solution-phase analysis as well as in a multifunctional sensory film preparation is presented. The interactions of AuNP with glutathione and homocysteine have been investigated using resonance elastic light scattering (RELS) and plasmonic UV-Vis spectroscopy. The high sensitivity of the RELS measurements enables monitoring of ligand exchanges and the biomarker-induced AuNP assembly. The viability of designing simple and rapid assays for the detection of glutathione and homocysteine is discussed. The surface plasmon band broadening and bathochromic shift are consistent with the biomarker-induced AuNP assembly and corroborate the RELS measurements and HR-TEM imaging. The results of molecular dynamics and quantum mechanical calculations support the mechanism of the formation of GSH- and Hcys-linkages in the interparticle interactions and show that multiple H-bonding can occur. In contrast to homocysteine and glutathione that induce gold nanoparticle assembly in specific pH ranges, no aggregation of nanoparticles has been

found in the presence of nitrotyrosine. The interactions of nitrotyrosine with gold nanoparticles and two fluorescent dyes with different spectral characteristics have also been investigated. These interactions result in changes in the resonance elastic light scattering (RELS) and fluorescence quenching that can be utilized in designing assays for the biomarker. The adsorption measurements of nitrotyrosine and coumarin 120 on a QC/Au quartz crystal piezoelectrode corroborate the observed RELS and static fluorescence quenching effects. Next, the novel molecularly-templated conductive polymer films are described. These films, utilized for the detection of various biomolecules, are mimicking the biorecognition processes occurring in nature, such as in the antibody-antigen interactions, or biotin-streptavidin binding. We have found that the functionalized gold nanoparticles enhance the response of molecularly-templated conductive polymer films for the detection of biomolecules and amplify the analytical signal through AuNP labeling. Novel designs of molecularly imprinted poly(orthophenylenediamine) sensor films are presented. The oxidative stress biomarker-induced assembly of monolayer-protected gold nanoparticles is evaluated in view of prospective applications of gold nanoparticles in designing inexpensive nanostructured sensors and microsensor arrays for field-deployable and point-of-care utilization.

2. Redox-potential homeostasis and protection against oxidative-stress

Glutathione and its oxidized disulfide form (GSSG) constitute the main redox regulation system in living organism's homeostasis. GSH protects cells against organic peroxides and damaging radicals, and is involved in signaling processes associated with cell apoptosis. The diminished active GSH levels in cells and body fluids lead to the reduced antioxidation capacity (Noble et al., 2005) to protecting against radicals and have been found to increase susceptibility to autism (Bernard et al., 2001, Clark-Taylor et al., 2004), diabetes (Beard et al., 2003), and other diseases (Almazan et al., 2000, Beard et al., 2003, Clark-Taylor et al., 2004, Clarkson, 1992, Noble et al., 2005, Polidoro et al., 1984, Repetto et al., 1996, Upadhya et al., 2004). The low GSH levels have been found to be caused by oxidative stress and exposure to toxic heavy metals (Hg, Cd, Pb). GSH and phytochelatines with general structure $(\gamma\text{-Glu-Cys})_n\text{Gly}$ participate as the capping agents (Barbas et al., 1992, Dameron et al., 1989) in heavy-metal sulfide nanoparticles formed in living organisms in natural detoxification processes (Inouhe, 2005, Mehra et al., 1991, Vatamaniuk et al., 2000, Vatamaniuk et al., 2001). While the kinetics of a systemic response to an oxidative stress is basically dependent only on the GSH level, the *redox potential* depends on both the GSH and GSSG. Still, the sensitivity of the redox potential to GSH level change is twice as high as that corresponding to the GSSG level change. This follows from the Nernst equation:

$$E = E^0 + 0.02958 \log [GSSG] - 0.05916 \log [GSH] - 0.05916\ pH \quad (1)$$

relating to the reaction equation for the redox process: $GSSG + 2H^+ + 2e^- = 2GSH$. In other words, the redox potential depends on the ratio: $(\sqrt{[GSSG]})/[GSH]$ rather than on the straight ratio: [GSSG]/[GSH]. The *redox buffering capacity* to both the oxidative and reductive stresses can be defined by the sum of concentrations: [GSH]+2[GSSG]. The factor 2 in this expression is due to the stoichiometry of the redox reactions in which GSSG can accept 2 electrons whereas GSH can give up 1 electron. If we consider the effectiveness of bodily response only to the oxidative stress then the *oxidative stress buffering capacity* would be better expressed by [GSH] alone rather than the concentration sum of GSH and

GSSG. Commonly used is also the *redox ratio* defined as: [GSH]/[GSSG] which is more convenient than the square root ratio discussed above.

3. Gold nanoparticle-based colorimetric assays for biomarkers of oxidative stress

The biomolecule-induced gold nanoparticle assembly process can be monitored using surface plasmon (SP) absorbance and SP band shifts. The oscillation frequency of the local surface plasmon is very sensitive to the changes in dielectric environment of nanoparticles and distance between nanoparticles. The collective oscillation of local surface plasmons is excited when the distance d between AuNP is: $d < 5r$, where r is the AuNP radius. Theoretical studies of plasmonic oscillations (Brioude et al., 2005, Draine et al., 1994, Gonzales et al., 2007, Jain et al., 2006, Kooij et al., 2006, Lee et al., 2005, 2006, Prescott et al., 2006, Ungureanu et al., 2009, Yang et al., 1995, Yin et al., 2006) and SP absorbance spectra (Alvarez et al., 1997, Etchegoin et al., 2006, Johnson et al., 1972, Kamat, 2002, Link et al., 1999a, Link et al., 1999b, Mishchenko et al., 2002, Perez-Juste et al., 2005, Ping et al., 2008) have enabled the understanding of mechanisms leading to the absorbance maximum shifts associated with the assembly processes. Extensive studies of the surface plasmon absorbance for various AuNP systems have been carried out by several groups (Alivisatos et al., 1996, Elghanian et al., 1997, Hostetler et al., 1998, Hostetler et al., 1999, Kamat, 2002, Kariuki et al., 2004, Kelly et al., 2003, Lim et al., 2009, Maye et al., 2005, Park et al., 2002 , Reynolds et al., 2000, Storhoff et al., 1998, Taton et al., 2000, Taton et al., 2001, Zheng et al., 2000). In this work, the formation of networks of fluorosurfactant ZONYL-capped spherical AuNP's mediated by Hcys, and glutaraldehyde molecules have been investigated (Scheme 1).

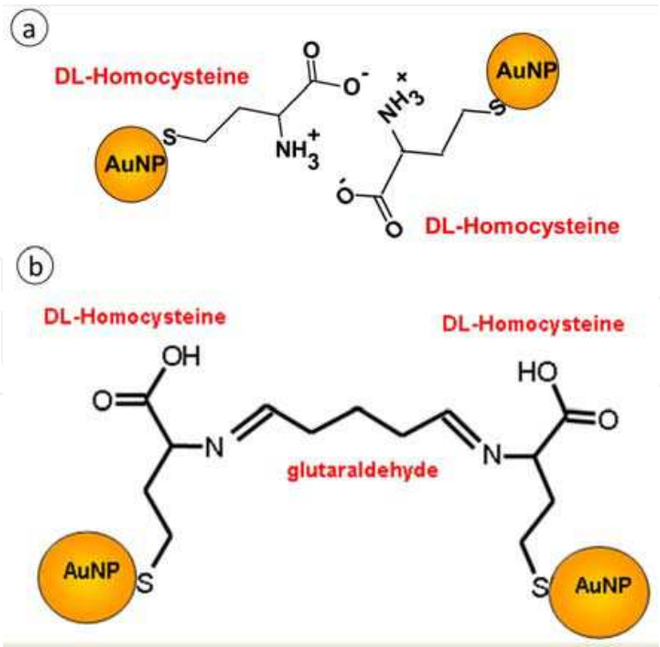

Scheme 1. Mechanisms of assembly of the gold nanoparticles: (a) Interparticle zwitterion-type electrostatic interactions between Hcys-capped AuNP; (b) Covalently-bonded glutaraldehyde nanobridge, linking Hcys-capped gold nanoparticles.

Fluorosurfactants provide similar advantages to other surfactants but, in addition, show high degree of chemical inertness. The ZONYL fluorosurfactant is known to form self-assembled monolayers on gold surfaces rendering the surface more hydrophobic and significantly retarding the gold oxide formation processes (Li et al., 2004). Although this surfactant forms water-tight shells, its bonding to a gold surface is not as strong as that of thiolates. Therefore, in presence of homocysteine, ZONYL is replaced in a ligand exchange process by thiol. The ligand exchange process taking place upon addition of homocysteine to ZONYL-capped AuNP solution can be monitored using SP band absorbance of AuNP (Figure 1 a). The UV–Vis spectra 1–9 were recorded for increasing concentrations of Hcys, from 0 to 22.2 μM and constant concentration of $AuNP_{5nm}$ (6 nM). It is seen that the SP band shifts toward longer wavelengths and the maximum absorbance increases with increasing C_{Hcys}. These observations are consistent with ligand exchange process:

$$AuNP/\ FES_x + yHcys = AuNP\ /Hcys_y + xFES \quad (2)$$

where FES denotes a fluorosurfactant molecule and $x \approx y$, followed by interparticle molecular linking of AuNP/Hcys through direct Hcys-Hcys interactions. At the pH =6.0, homocysteine exists as a zwitterion with α-amino group protonated ($-NH_3^+$) and carboxylic group dissociated (COO^-). Therefore, the zwitterionic interparticle binding between Hcys-capped AuNP is playing a predominant role, as recently discussed by Zhong et al. (Lim et al., 2007). The bathochromic shift of the surface plasmon peak ($\Delta\lambda_{max}$ = 36 nm, for 16 μM Hcys) corresponds to the formation of small Hcys-linked AuNP ensembles. The increase of SP absorbance by 21% (from 0.253 to 0.305) indicates on the collective oscillations of local surface plasmons in AuNP that form these ensembles. The absorbance maximum increases with C_{Hcys} and reaches the saturation value at $C_{Hcys} > 7$ μM, with the half-absorbance change appearing at $C_{Hcys} = 3.38$ μM. The value of λ_{max} also reaches saturation at $C_{Hcys} > 7$ μM (Figure 1b). Therefore, we can assume that above 7 μM Hcys concentration the ligand exchange process has completed and nanoparticle shells are saturated with Hcys.

At neutral solutions, Hcys-capped AuNP do not assemble. In the following, we present a method for Hcys-capped AuNP assembly by interparticle crosslinking using glutaraldehyde as the linker (Scheme 1b). The linking is achieved through the condensation reaction between aldehyde groups of glutaraldehyde and amine groups of Hcys, with the formation of covalent amide bonds. The UV-Vis spectra were recorded for increasing concentrations of Hcys, from 0 to 30 μM, while maintaining the concentration of $AuNP_{5nm}$ constant (2.53 nM), as illustrated in Figure 2a. The concentration of glutaraldehyde was also maintained constant (1.12 %). These spectra show a bathochromic shift of the SP peak from 517.4 to 562.3 nm for 0 and 20 μM Hcys, respectively, with $\Delta\lambda$ = 44.9 nm (Figure 2b). It corresponds to the formation of glutaraldehyde-linked Hcys-capped AuNP ensembles. The surface plasmon band shift toward longer wavelengths is consistent with the assembly of Hcys-capped gold nanoparticle networks by glutaraldehyde interparticle linker. The increase of SP absorbance by 21% (from 0.24 to 0.29 for 20 μM Hcys) indicates on the excitation of collective oscillations of local surface plasmons in AuNP that form these ensembles.

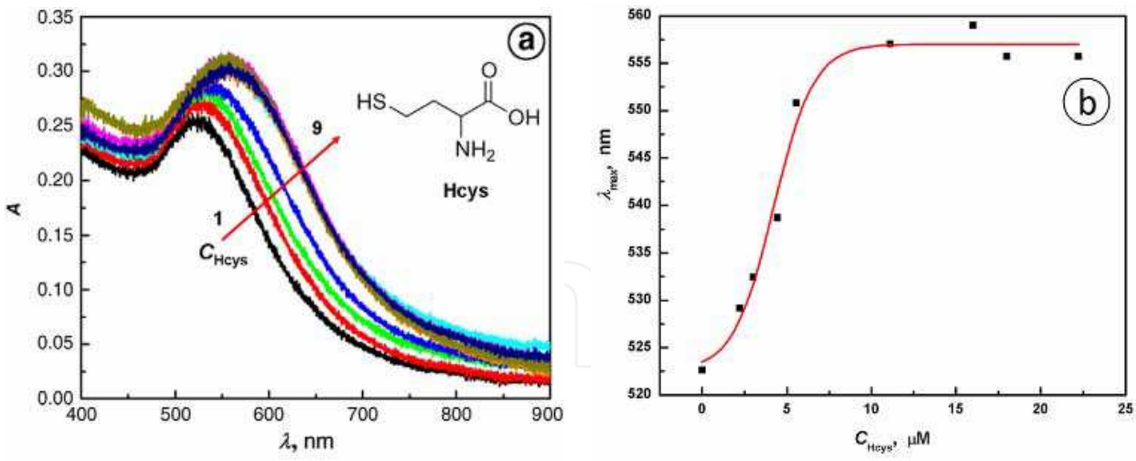

Fig. 1. (a) Absorbance spectra for ZONYL-capped AuNP for different concentrations of homocysteine, C_{Hcys} [μM]: (1) 0, (2) 2.22, (3) 3, (4) 4.44, (5) 5.56, (6) 11.11, (7) 16, (8) 18, (9) 22.22; C_{AuNP} = 6 nM, C_{ZONYL} = 0.22 %, pH = 6; (b) dependence of λ_{max} vs. C_{Hcys}.

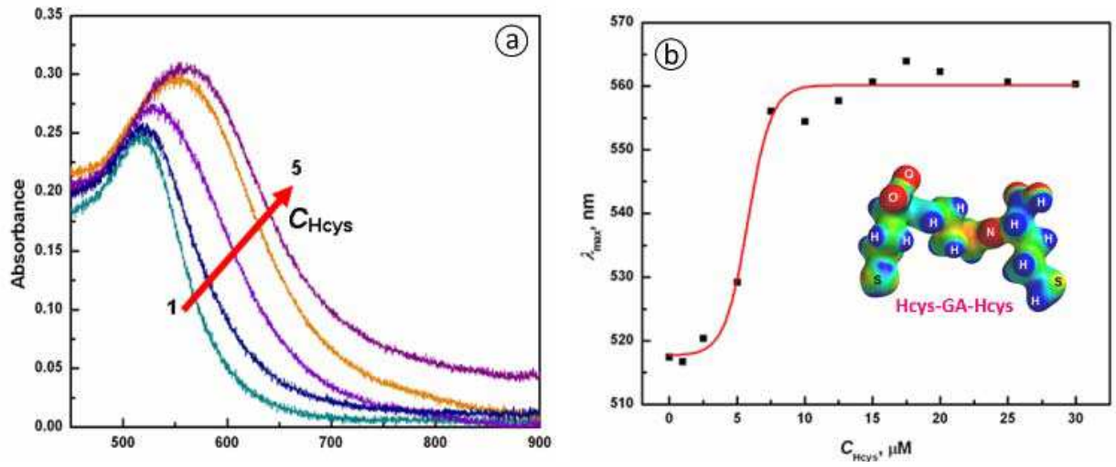

Fig. 2. (a) Absorbance spectra for glutaraldehyde linked homocysteine-capped AuNP for different concentration of DL-homocysteine, C_{Hcys}, μM: (1) 0, (2) 2.5, (3) 5, (4) 10, (5) 15. C_{AuNP} = 2.53 nM, C_{GA} = 1.12%, pH = 7; (b) Dependence of λ_{max} vs. C_{Hcys} for glutaraldehyde-linked AuNP@Hcys.

4. Biomolecule-induced gold nanoparticle assembly studied by RELS

The oxidative stress has been suggested as the causative factor in aging (Carlo et al., 2003) and many diseases such as cardiovascular, cancer, autism spectrum disorders (ASD) (James et al., 2006), and others. Among the biomarkers of oxidative stress are small biomolecules such as: ubiquinol (Yamamoto et al., 2002) which is very labile in the oxidation of low-density lipoprotein (LDL), glutathione (GSH) which is depleted in the presence of organic radicals and peroxides (Droge, 2002), homocysteine (Carmel et al., 2001, Jacobsen, 2000) which has been found at elevated levels in atherosclerosis (Boushey et al., 1995, Graham et al., 1997, Lentz et al., 2004, Refsum et al., 1989, Welch et al., 1998, Zhang et al., 2000),

Alzheimer disease (Seshadri et al., 2002, Varadarajan et al., 2001), dementia (Seshadri et al., 2002), and poses an increased risk of birth defects (Mills et al., 1996). Some biomarkers of oxidative stress are necessary to maintain healthy homeostasis (e.g. glutathione), while others participate in the development of diseases (e.g. homocysteine). There is now mounting evidence that oxidative and nitrosative stress resulting from hyperglycemia is involved in the development of diabetes and is implicated in the micro- and macrovascular complications of the disease. Such biomarkers of oxidative stress as nitrotyrosine and homocysteine show elevated levels and glutathione shows a decreased level in a progressing disease. In this study, the interactions of nitrotyrosine, homocysteine and glutathione with gold nanoparticles have been investigated. These interactions result in changes in the resonance elastic light scattering (RELS) that can be utilized in designing assays for the biomarker. Since the RELS spectroscopy offers an exceptional sensitivity to the AuNP assembly, we have employed the RELS measurements to determine if there is any aggregation of AuNP taking place in the presence of NT and Hcys. In Figure 3a, the synchronous full-scan RELS spectra recorded after addition of NT to cysteamine-capped AuNP are presented.

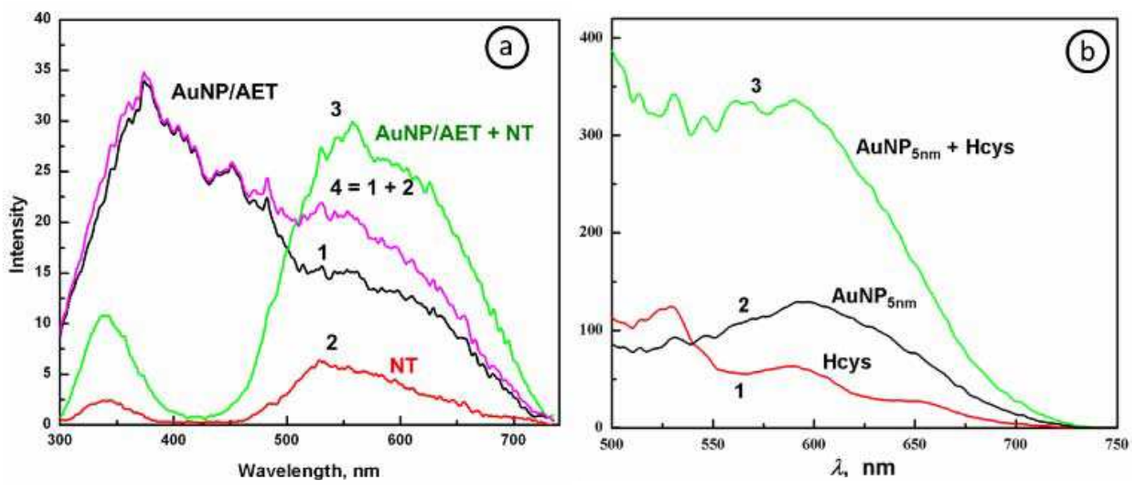

Fig. 3. Synchronous scan RELS spectra for: (a) (1) 0.95 nM cysteamine-capped $AuNP_{5nm}$, (2) 0.33 mM NT, (3) 0.95 nM cysteamine-capped $AuNP_{5nm}$ + 0.33 mM NT, (4) sum of spectra (1) and (2); 20 mM TrisHCl buffer, pH = 7.4. (b) (1) 20 μM Hcys, (2) 3.8 nM $AuNP_{5nm}$ and (3) 3.8 nM $AuNP_{5nm}$ + 20 μM Hcys recorded after 60 s reaction time.

The spectrum in curve 3 shows a decrease of RELS intensity upon addition of NT in the short wavelength region (300 - 500 nm) and an increase of RELS intensity in the long wavelength range (500 - 700 nm) in comparison with the spectrum of cysteamine–capped gold nanoparticles (Figure 3a, curve 1). The quenching of the light by NT molecules at shorter wavelengths indicates that a screening of gold nanoparticles by amino acid occurs. Curve 4 represents the theoretical sum of spectra for nanoparticles and NT (curve 1 and 2, respectively). This spectrum can be directly compared with spectrum which was recorded for 0.33 mM NT in the presence of 0.95 nM cysteamine–capped AuNP (curve 3). It is clear that the spectra for AuNP and for NT are not additive. This indicates on the formation of supramolecular assemblies. For AuNP@Hcys (Figure 3b), well resolved RELS spectra were obtained for excitation wavelengths in the range: λ_{ex} = 500 – 650 nm. The full-scan RELS spectra for citrate capped gold nanoparticles and Hcys mixture show the increase of RELS

intensity of AuNP@Cit upon addition of homocysteine in the entire range of scanned wavelength. The increase of scattering intensity is due to the dependence of scattering cross-section on particle diameter a and the dielectric function (or refractive index) of the medium.

$$I_{sc} = I_0 N \frac{\left(1+\cos^2\theta\right)}{2R^3}\left(\frac{2\pi}{\lambda}\right)^4 \frac{\left[\left(n_p - n_s\right)^2 - 1\right]}{\left[\left(n_p - n_s\right)^2 + 2\right]}\left(\frac{a}{2}\right)^6 \tag{3}$$

where n_p and n_s are the refractive indices for the particles and the solution, respectively, λ is the wavelength of incident light beam, R – the distance from source, θ - the scattering angle, N - the number of particles, and I_0 is the constant.

The addition of NT to the cysteamine-capped $AuNP_{5nm}$ nanoparticles results in the enhancement of Rayleigh scattering for the excitation wavelength λ_{ex} = 560 nm, as indicated in Figure 4a, curves 2-5, obtained for 0.95 nM $AuNP_{5nm}$ + x μM NT, where x = 0 ... 333 μM. This confirms that supramolecular assemblies are formed. At 7.4, citrate ions stabilize gold colloids by forming tight negatively charged shells around nanoparticles cores ($pK_{a,1}$ = 3.09, $pK_{a,2}$ = 4.75, $pK_{a,3}$ = 5.41). After the addition of cysteamine to the solution of citrate-capped AuNP, citrates are replaced in a ligand exchange process by thiols. At pH 7.4 α-amino group of cysteamine are protonated ($-NH_3^+$) and form positively charged shells around the gold nanoparticles cores. At pH > 6.8, the deprotonation of hydroxyl group of NT is observed and NT exists as an anion (pK_{a1} = 2.20, pK_{a2} = 6.8, pK_{a3} = 9.11). Hence, the NT molecules are electrostatically attracted to AuNP@AET and supramolecular structure by electrostatic interactions and hydrogen bonding between $-COO^-$ and $-NH_3^+$ of NT molecules and cysteamine-capped gold nanoparticles AuNP@AET can be formed. Upon addition of homocysteine to citrate-capped AuNP, an increase in resonance elastic light scattering is also observed (Fig. 4b). The RELS spectra were obtained at pH = 5.0 for λ_{ex} = 560 nm, for increasing concentrations of Hcys from C_{Hcys} = 0 to 15 μM. The pK_a values for Hcys are: pK_1 = 2.22 (-COOH), pK_2 = 8.87 ($-NH_2$) and pK_3 = 10.86 (-SH)) making it a zwitterion at pH = 5. As the ligand exchange process progresses, the citrate ions are being replaced by the neutral Hcys molecules. The progression is accelerated at higher Hcys concentrations. The switching begins at C_{Hcys} = 4μM and ends at C_{Hcys} = 6μM with a sharp transition from the background scattering level of AuNP@Cit to that characteristic of the AuNP@Hcys. Similar RELS experiments carried out for other aminoacid ligands and glutathione show that the RELS response is highly selective to Hcys leading for analytical determinations of homocysteine in a matrix of aminoacids and glutathione. In the presence of GSH, at pH = 3.24 ± 0.03, the light scattering from $AuNP_{5nm}$ nanoparticles is also strongly enhanced (Fig. 4c). The RELS signal, measured within 1 min of reaction time, depends on GSH concentration and increases monotonously with C_{GSH} from $I_{sc,0}$ = 7.34 for the 0 mM to $I_{sc,max}$ = 66.14 for the 5 mM concentration of the glutathione solution. At this pH, the GSH is predominantly neutral (zwitterionic) form and may caused aggregation of AuNP. pKa values for GSH are: pK_1 = 2.04 (glutamate –COOH), pK_2 = 3.4 (glycine –COOH), pK_3 = 8.72 (–SH group), pK_4 = 9.49 (–NH_2 group). The enhancement of RELS from $AuNP_{5nm}$ by GSH molecules is attributed to the size increase of AuNP due to the ligand exchange (i.e. replacing short-chain citrate molecules in the nanoparticle shell with longer-chain GSH molecules) and interparticle interactions leading to AuNP assembly.

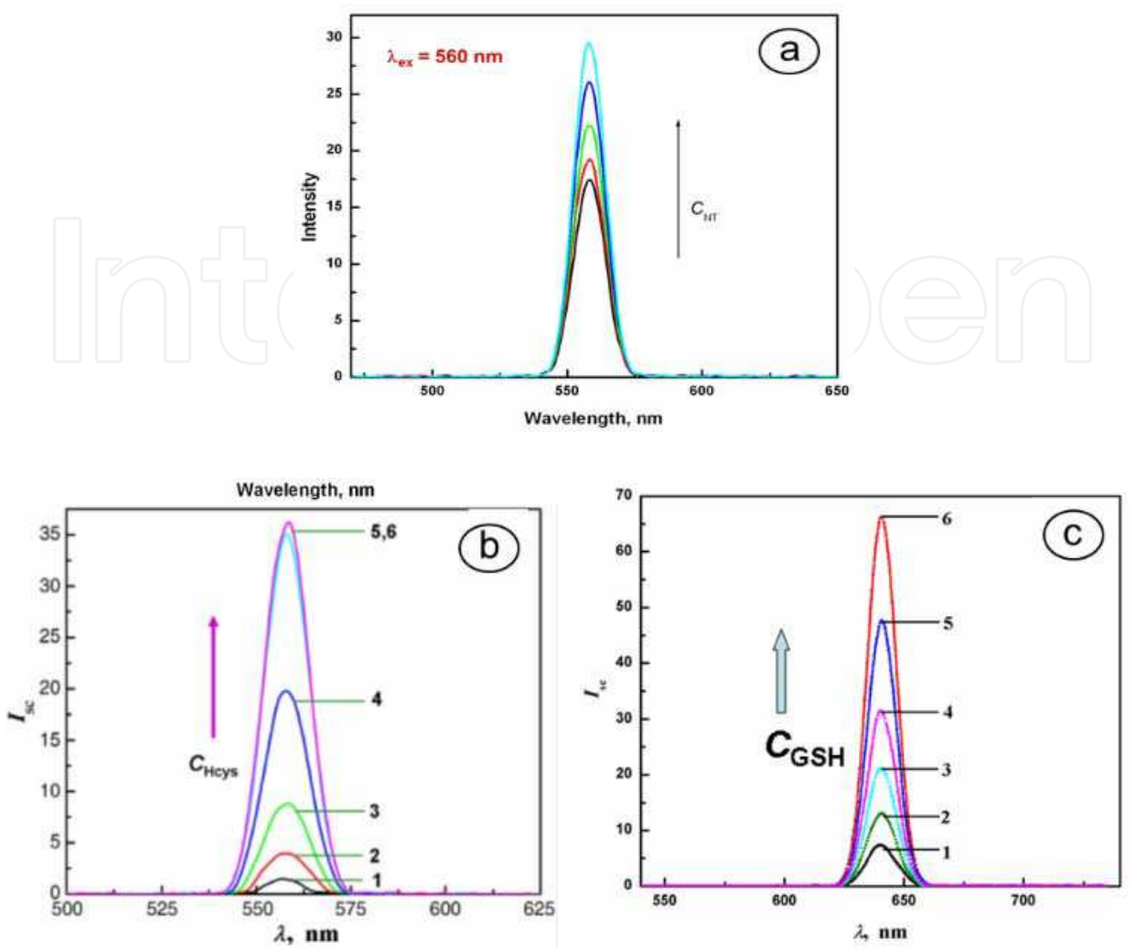

Fig. 4. (a) Dependence of RELS spectra for 0.95 nM cysteamine-capped $AuNP_{5nm}$ + x μM NT, x [μM]: (1) 0, (2) 83.3, (3) 166.7, (4) 250, (5) 333; λ_{ex} = 560 nm; 20 mM TrisHCl buffer, pH = 7.4; (b-c) Resonance elastic light scattering spectra for citrate-capped $AuNP_{5\ nm}$ for different concentrations of (b) homocysteine and (c) glutathione, C_{Hcys} [μM]: (1) 0, (2) 5, (3) 5.5, (4) 5.75, (5) 6.75, (6) 15, C_{AuNP} = 3.8 nM, pH = 5, λ_{ex} = 560 nm; C_{GSH} [mM]: (1) 0, (2) 2.67, (3) 3.0, (4) 3.17, (5) 3.33, (6) 5, C_{AuNP} = 10.1 nM.

In contrast to the behavior of NT, Hcys and GSH, replace nonthiolated AuNP shell and in the proper pH range induce assembly of gold nanoparticles (Figure 5) (Lim et al., 2007, Lim et al., 2008, Stobiecka et al., 2010a, Stobiecka et al., 2010b). Large increase of the RELS signal was reported for both GSH and Hcys confirming the assembly process (Stobiecka et al., 2010a, Stobiecka et al., 2010b). While in the Hcys-induced assembly, the main forces are H-bonding, in the case of GSH-induced assembly, the zwitterionic forces are dominant, although the H-bonding plays also a role (Lim et al., 2007, Lim et al., 2008). No aggregation of nanoparticles has been found in the presence of nitrotyrosine.

Taking into account the decrease in particle concentration due to assembly and assuming λ = const, the increase of the effective particle diameter a_{rel} can be estimated using the formula:

$$a_{rel} = \frac{a_1}{a_0} = \sqrt[3]{\frac{I_{sc,1}}{I_{sc,0}}} \tag{4}$$

where indices 0 and 1 stand for the particles before and after NT addition, respectively. From the data of Figure 4a, the scattering intensity increase is: $I_{sc,1}/I_{sc,0}$ = 1.695 and, hence, a_{rel} = 1.192. This increase in a_{rel} is relatively small and indicates that aggregates of AuNP are not formed, otherwise the value of $a_{rel} \geq 2$ should be obtained (Stobiecka et al., 2010a, Stobiecka et al., 2010b). Therefore, the increase in particle diameter observed upon interactions of AuNP with NT is due to the attachment of NT to the outer interface of the AET-capped AuNP shell. The increase in scattering intensity upon addition of 15 μM Hcys is $I_{sc,1}/I_{sc,0}$ = 36.2/1.91=19.0 (mean of 5 measurements) (Fig 4b). The 19-fold increase in scattering intensity clearly indicates on the homocysteine-induced assembly of AuNP. Utilizing Eq. (4), we obtain for the increase of particle diameter: a_{rel} = 2.7. From the data of Figure 4c, the scattering intensity increase after addition of the 5 mM GSH is: $I_{sc,1}/I_{sc,0}$ = 9.01 and, hence, a_{rel} = 2.08. This means that most likely small aggregates composed of only few nanoparticles (e.g 2-6) are formed.

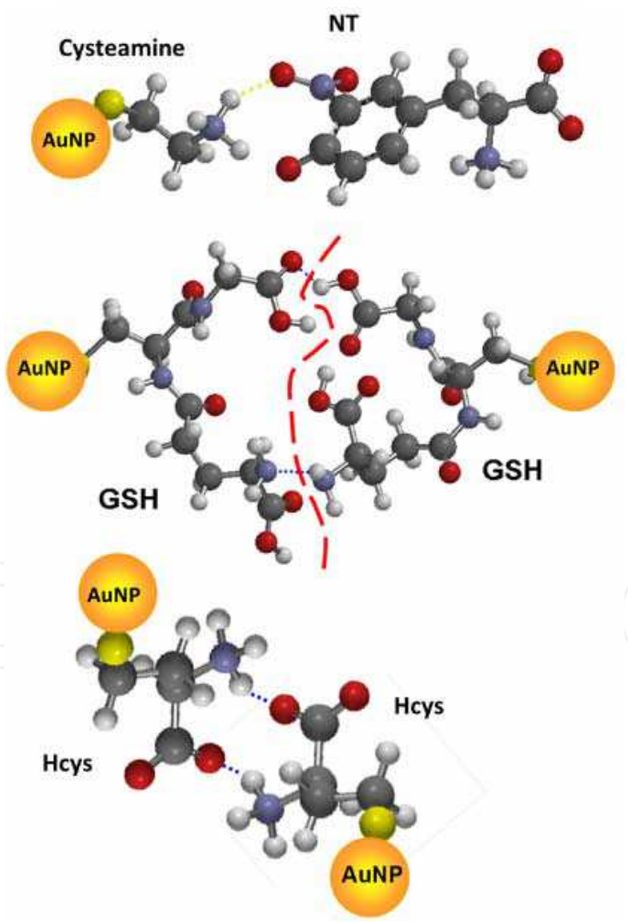

Fig. 5. Hydrogen bonding between AuNP@AET and NT, two glutathione/homocysteine molecules from shells of two interacting AuNP and ; H-bonds marked with a dotted line; atoms: yellow – sulfur, red –oxygen, blue – nitrogen, gray – carbon, light gray – hydrogen).

5. Ligand-exchange processes in core-shell nanoparticle systems

Growing interests in bioassays providing transduction of bioinformation to optical and electronic signals have recently been observed in conjunction with stimulating developments in synthesis of highly efficient quantum-dots and functionalized gold nanoparticles (AuNP) (Bain et al., 1989, Hostetler et al., 1999). Kinetic studies show that ligand-exchange process in a self-assembled monolayer (SAM) film is basically a Langmuirian pseudo-first-order process and is based on the random place-exchange proceeding evenly on the entire surface of AuNP. This process may be influenced by such slow steps as surface diffusion, hydrogen bond breaking, or slow desorption. The improvement of the rate of metal nanoparticle functionalization is then highly desired. In this work, we have described phenomena which are the key factors for the design of biosensors with fabrication of nanoparticle-enhanced sensory film and other applications such as the photodynamic cancer therapy or colorimetric assays for heavy metals. These phenomena relate to the speed of the film formation and modification of the film composition. In the proposed methodology, we have employed a biomolecule, homocysteine (Hcys), as the ligand replacing citrate capping of $AuNP_{5nm}$ and glutathione (GSH) which can act as the moderator for one-step ligand-exchange processes. The ultra-fast functionalization of gold nanoparticles process was monitored using RELS spectroscopy. It proceeds through the nucleation and avalanche growth of ligand-exchange domains in the self-assembled monolayer film on a gold nanoparticle surface (Scheme 2).

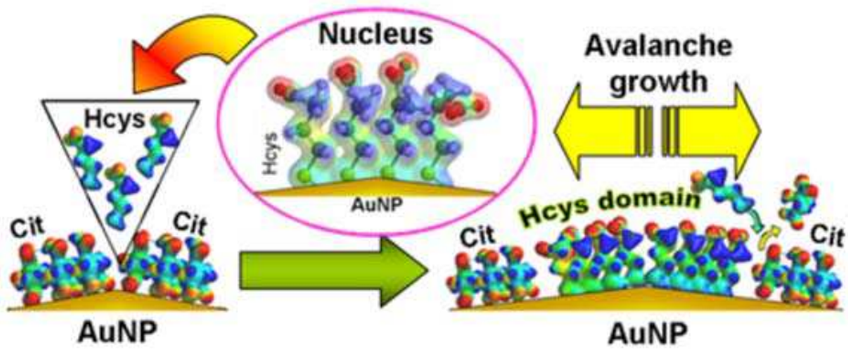

Scheme 2. Schematic view of the hydrogen bonded citrate SAM basal film and the nucleation and growth of a hydrogen bonded Hcys-ligand domain on an edge of a citrate-capped AuNP.

To distinguish between Hcys-dominated AuNP and GSH-dominated AuNP, the pH dependence of RELS was analyzed. By carefully selecting pH, it is possible to keep Hcys in the form of zwitterions, which leads to the AuNP assembly (Figure 6). In solution at pH = 5, we have predominantly zwitterionic Hcys and negatively charged GSH. Therefore, a high RELS intensity can be ascribed to the Hcys-dominated AuNP shells (due to Hcys-induced aggregation of AuNP's) and low RELS intensity to the GSH-dominated AuNP shells (due to repulsions between AuNP's).

The ability to control the SAM composition in the fast ligand-exchange process is the key element to the nanoparticle functionalization. The mechanism of action of the moderator molecules is not well understood but it likely involves the competition for the nucleation sites and/or tuning the exchange processes at ligand-exchange wave-front, i.e. at the perimeter of the growing domains of the incoming ligand. To control the SAM composition

in the fast ligand-exchange process, GSH-moderator molecules able to influence the nucleation and growth processes in the short time-scale of the functionalization process have been used. A series of experiments has been performed in which the concentration ratios C_{GSH}/C_{Hcys} were changed in a wide range from 0.002 to 160. In Figure 7, the RELS intensity for 3.8 nM $AuNP_{5nm}$ solutions is plotted vs. C_{Hcys} for different concentration levels of GSH.

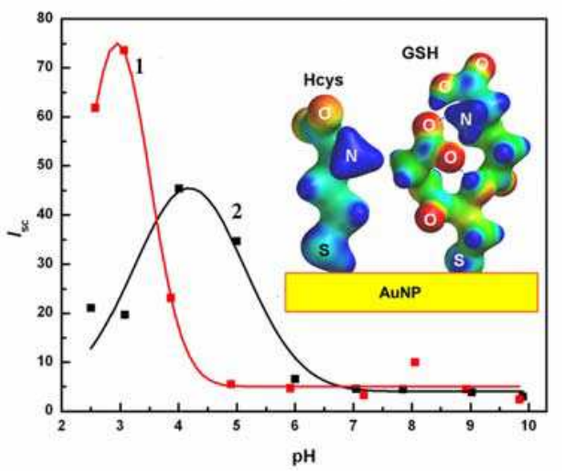

Fig. 6. Dependence of I_{sc} on pH for: (1) 20 μM GSH solutions and (2) 20 μM Hcys solutions; τ = 60s; C_{AuNP} = 3.8 nM; AuNP diameter: 5 nm, C_{Cit} = 0.46 mM.

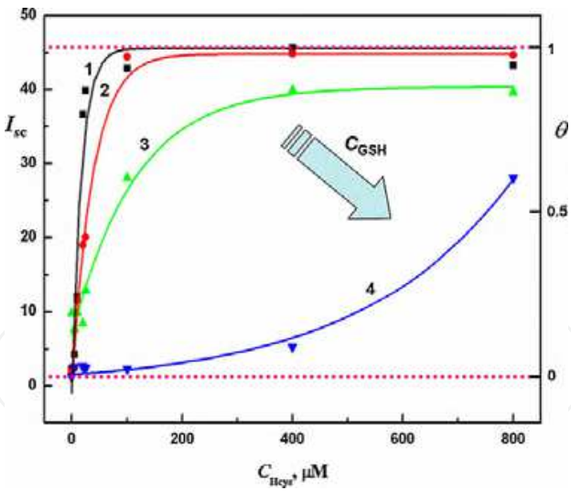

Fig. 7. Tuning the speed of ligand-exchange and SAM shell composition in fast AuNP functionalization; dependence of RELS intensity I_{sc} on C_{Hcys} for different C_{GSH} [μM]: (1) 5, (2) 20, (3) 100, (4) 400; C_{AuNP} = 3.8 nM, citrate buffer, C_{Cit} = 0.46 mM, pH= 5, λ_{ex} = 640 nm, τ = 60 s; all curves are fitted with sigmoidal Boltzmann function.

The average composition of the film is approximately given by:

$$\theta = \frac{(I - I_{\min})}{(I_{\max} - I_{\min})} \tag{5}$$

where θ is the content of the linker ligand (Hcys) in the SAM shell and I_{min}, I_{max} are the minimum and maximum scattering intensities corresponding to AuNP@GSH and AuNP@Hcys, respectively. This dependence enables a quick estimate of the average film composition.

The changes in film composition, are useful in several approaches in sensory film fabrication, such as in the process of: (i) embedding two, or more, different functionalities, (ii) introducing spacers for the attachment of large bioorganic molecules, or (iii) controlling the range of sensor response. On the other hand, no morphological changes in nanoparticle cores are encountered unless the system is heated to higher temperatures, which would result in AuNP core enlargement.

The aggregation of AuNP may also be caused by other factors, such as the addition of higher salt concentrations or injection of small amounts of multivalent metal cations able to coordinate to the ligands of nanoparticle shells, however, neither the salt or metal cations have any chance to replace a SAM film that protects AuNP. The affinity of thiols to a Au surface (Whitesides et al., 2005) enables such thiols as GSH and homocysteine to readily replace citrates from the nanoparticle shell (Lim et al., 2007, Lim et al., 2008, Stobiecka et al., 2010b). While GSH can form intermittently some weakly bound intermediate interparticle linking structures (Stobiecka et al., 2010a), these only help to isolate a citrate ion from its neighbors and remove that citrate from the film.

6. Bio-inspired molecularly-templated polymer films for biomarker detection

The strong affinity observed in host-guest recognition systems in biology, such as the antibody-antigen, receptor-protein, biotin-streptavidin, or DNA-polypeptide, has been widely utilized in designing various biosensors and assays for analytical determination of biomolecules of interest. The recently developed methods for bioengineering of aptamers based on oligonucleotides or polypeptides (Hianik et al., 2007, Tombelli et al., 2005) as ligands mimicking host molecules in biorecognition systems shows that aptamers can be used in sensors for various target (guest) molecules. The bioengineered aptamers provide some advantages over natural host-guest systems, including higher packing density and improved structural flexibility. Another bio-inspired host-guest system studied extensively is based on molecular imprinting of polymer films (Greene et al., 2005, Levit et al., 2002, Perez et al., 2000, Piletsky et al., 2001, Priego-Capote et al., 2008, Yan et al., 2005, Ye et al., 2000) whereby the polymerization of a polymer is carried out in the presence of guest molecules. The latter are then released from the template, e.g. by hydrolysis. The templated polymer films specific toward the target molecules are inexpensive and offer enhanced scalability, flexibility, and processibility. Hence, the molecularly-imprinted polymers are good candidates for sensor miniaturization and the development of microsensor arrays. The templated polymers show recognition properties resembling those found in biological receptors but they are more stable and considerably less expensive than biological systems (Malitesta et al., 2006).

A range of molecularly-imprinted polymer-based sensors have been investigated using different transduction techniques, including: acoustic wave (Kikuchi et al., 2006, Kugimiya et al., 1999, Liang et al., 2000, Matsuguchi et al., 2006, Percival et al., 2001, Tsuru et al., 2006, Yilmaz et al., 1999), potentiometry (Javanbakht et al., 2008), capacitance (Panasyuk et al., 1999), conductometry (Kriz et al., 1996, Sergeyeva et al., 1999), voltammetry (Prasad et al., 2005), colorimetry (Stephenson et al., 2007), surface plasmon spectroscopy (Tokareva et al.,

2006), and fluorescence (Chen et al., 2004, Chen et al., 2006, Jenkins et al., 2001, Moreno-Bondi et al., 2003) detection. Moreover, the molecularly-imprinted polymers can also be utilized for selective solid-phase separation techniques (Mahony et al., 2005, Masque et al., 2001), including electrophoresis and chromatography. Furthermore, it has been found that the analytical signal can often be enhanced by employing nanoparticle labeling of guest molecules (Stobiecka et al., 2009).

The key role in accomplishing the desired target recognition level is played by the synthesis of templated-polymer films. A polymer with appropriate functionalities has to be selected to provide effectively multiple binding sites for a target molecule. Therefore, the target molecules should interact with monomers during the polymerization stage and act as a template around which the polymer grows. Following the release of templating molecules, the high affinity sites should remain in the polymer matrix, constituting the host architecture for supramolecular interactions of the host with the guest molecules. The methods of molecular imprinting mainly utilize a non-covalent imprinting which is more versatile and easier than the covalent imprinting. Various forms of non-covalent binding have been explored, including hydrogen bonding, Van der Waals forces, electrostatic or hydrophobic interactions.

As an example of the design of a molecularly-imprinted sensor film, we describe in this section a sensor for the biomarker of oxidative stress, glutathione. The molecular imprinting of GSH has been performed by electropolymerization of orthophenylenediamine (oPD) in the presence of the target molecules. The templated polymer films of poly(orthophenylenediamine), or PoPD, was formed in situ on a gold-coated quartz crystal resonator wafer (QC/Au) which enabled using the Electrochemical Quartz Crystal Nanobalance (EQCN) for monitoring the polymerization process, as well as for testing the sensor response to the target analyte. The EQCN technique (Hepel, 1999) can serve as a very sensitive technique to monitor minute changes in the film mass and has recently been applied in a variety of systems to study the film growth (Hepel et al., 2002, Stobiecka et al., 2011) and dissolution (Hepel et al., 2006, Hepel et al., 2007), as well as ion dynamics and ion-gating (Hepel, 1996, Hepel et al., 2003) in intercalation process allowing one to distinguish between moving ions on the basis on their molar mass differences.

The design of a GSH-templated polymer film is presented in Figure 8.

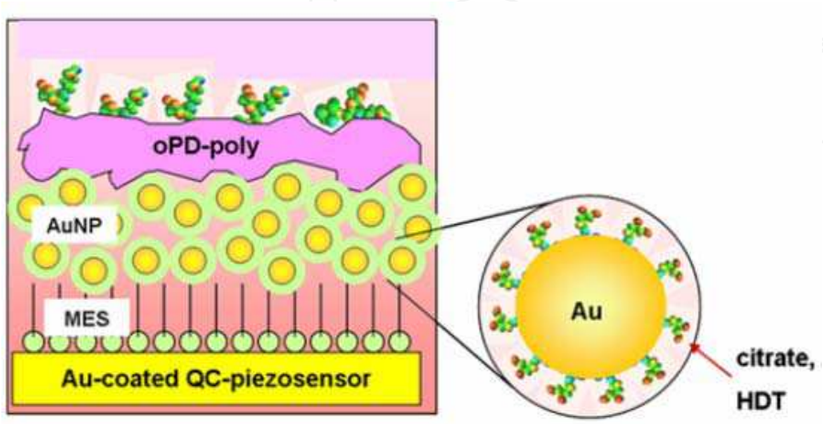

Fig. 8. Schematic of GSH-templated sensor design: GSH embedded in a PoPD film electrode-posited on a layer of AuNP network assembled on a SAM of MES on a Au piezoelectrode.

The sensor, QC/Au/AuNP/PoPD(GSH), was synthesized by direct electropolymerization of oPD in the presence of GSH, on a QC/Au substrate that was coated with a SAM of MES and a layer of HDT-capped AuNP network assembled on top of the SAM. The GSH molecules attached to the polymer surface at the end of the oPD polymerization stage leave impressions in the film which can be utilized for GSH detection. The disassociation of the templating GSH molecules is usually done by hydrolysis of GSH in 0.1-0.5 M NaOH solution.

Typically, the electropolymerization of PoPD is carried out either by successive potential scans from E_1 = 0 to E_2 = +0.8 V and back0020to E_1, or by potential pulses with E_1 = 0 to E_2 = +0.8 V and E_3 = 0, with pulse widths τ_1 = 1 s, τ_2 = 300 s.

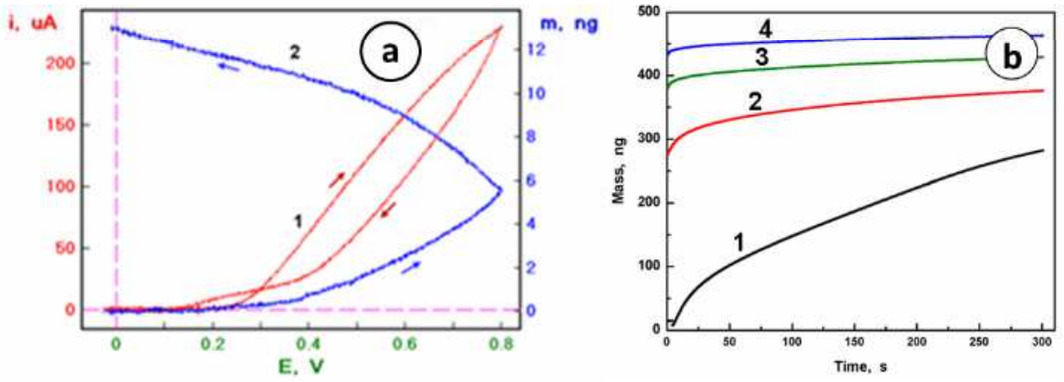

Fig. 9. (a) LSV and EQCN characteristics (first cycle) for a QC/Au electrode in 5 mM oPD + 10 mM GSH in 10 mM phosphate buffer solution: (1) current-potential, (2) mass-potential; v = 100 mV/s; (b) Apparent mass gain recorded in consecutive cycles of a potential-step electropolymerization of a GSH-templated poly(oPD) films from 5 mM oPD solutions containing 10 mM GSH; substrate: QC/Au/MES/AuNP; medium: 10 mM $HClO_4$; potential program: step from E_1 = 0 to E_2 = +0.8 V *vs* Ag/AgCl and back to E_1, pulse duration τ_1 = 1 s, τ_2 = 300 s; curve numbers correspond to the cycle number.

In simultaneous linear potential scan voltammetry (LSV) and nanogravimetry, we have found that the instant of the oPD oxidation is at E = 0.25 V vs. Ag/AgCl, followed by almost linear current increase in the potential range from E = +0.3 to +0.6 V. The apparent mass has been found to increase during the anodic potential scan. Further mass gain is also noted after the potential scan reversal. Moreover, we have found that the mass keeps increasing even after the current cessation at the end of the cathodic-going potential scan, at potentials E < +0.15 V. This clearly indicates on the formation of oPD radicals which are able to attach to the PoPD film after the oPD oxidation has ended. This mechanism is corroborated by the observed low Faradaic efficiency of the polymer formation caused by the diffusion of oPD intermediates and oligomeric radicals out of the electrode surface. The Faradaic efficiency can be investigated using the mass-to-charge analysis using the plots of apparent mass m versus charge Q. The experimental slope, $p_{exp} = \partial m/\partial Q$, is then compared to the theoretical slope p_{th} calculated for a given reaction as follows:

$$m = M\frac{Q}{nF} \tag{6}$$

$$p_{th} = \frac{\partial m}{\partial Q} = \frac{M}{nF} \tag{7}$$

where M is the *reaction molmass* reflecting the molar mass gain or loss of the electrodic film, F is the Faraday constant (F = 96,485 C/equiv) and n is the number of electrons transferred. For the reaction of electro-oxidation of oPD, we have:

$$C_6H_4(NH_2)_2(aq) - 4e^- = [\bullet N\text{-}C_6H_4\text{-}N\bullet] + 4H^+ \tag{8a}$$

$$C_6H_4(NH_2)_2(aq) - 4e^- = [\bullet N\text{-}C_6H_4\text{-}NH\bullet^+] + 3H^+ \tag{8b}$$

$$C_6H_4(NH_2)_2(aq) - 4e^- = [\bullet NH^+\text{-}C_6H_4\text{-}NH^+\bullet] + 2H^+ \tag{8c}$$

$$C_6H_4(NH_2)_2(aq) - 2e^- = [\bullet N\text{-}C_6H_4\text{-}NH_2\bullet] + 2H^+ \tag{8d}$$

oPD *PoPD unit*

where polymer chains with either closed phenazine moieties (8*a*-8*c*) or open phenazine (or quinoid) rings (8*d*) are formed. Assuming that the former dominate, we have the average molmass M_{ave} = 105 g/mol (i.e. the molar mass of species deposited on the electrode minus molar mass of species detached from the electrode surface; M ranges from 104 to 106 depending on the degree of nitrogen protonation) and n = 4. Equations (8) describe the oxidized PoPD units cross-linked to the electrodic polymer film. Under these conditions, the theoretical value of p is: p_{th} = 262 ng/mC (525 ng/mC for reaction (8d)). In comparison to that, the experimental values of p are much lower: p_{exp} = 7.1 ng/mC. This means that a large majority of the oxidized oPD radicals can escape to the solution before being able to bind to the electrode surface and become part of it. The polymerization efficiency does not increase in subsequent potential cycles.

In the potential step experiments, the potential program included 3 stages: E_1 = 0, E_2 = +0.8 V, and E_3 = 0, with pulse widths τ_1 = 1 s, τ_2 = 300 s. Generally, the current decayed monotonically and the apparent mass was increasing from the first moment of the step to E_2, as expected. The total mass increase observed in these experiments was much larger than that in the potential scan experiments and the analysis of p_{exp} indicates that the Faradaic efficiency ε is also higher (p_{exp} = 13.7 ng/mC) although still very low.

The number of PoPD monolayers deposited during the polymerization procedure can be estimated by calculating an equivalent monolayer mass of PoPD. Since the definition of the equivalent monolayer is rather ambiguous because the benzene rings of oPD may not be in plane or stacked parallel to each other in the PoPD (Stobiecka et al., 2009), we define the equivalent PoPD monolayer as a densely packed layer of flat oPD molecules. The calculated surface area for a unit oPD A = 27.1 Å^2 is assumed on the basis of quantum mechanical calculation of the electronic structure of the polymer (Stobiecka et al., 2009). Then, the maximum surface coverage is: Γ = 3.69 × 10^{14} molec/cm^2 and γ = 0.61 nmol/cm^2. The monolayer mass is then: m_{mono} = 65.0 ng/cm^2 and for our quartz resonator: $m_{mono,QC}$ = 16.6 ng/QC. Therefore, in a single potential scan experiment only a fraction of the equivalent PoPD monolayer is being formed.

Recent studies have shown that the polymer is mainly constituted by phenazinic and quinonediimine segments with different protonation levels (Sestrem et al., 2010). The formation of different crosslinks is illustrated in Scheme 3

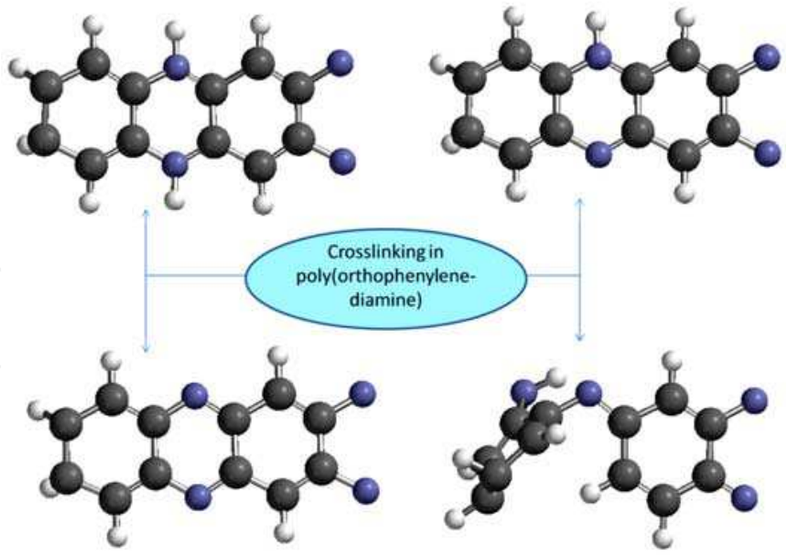

Scheme 3. Crosslinking in PoPD (adapted from (Sestrem et al., 2010)).

These experiments confirm that the GSH-templated films can be grown step by step under different conditions with straightforward control of the film thickness and its conductance by a simple choice of the pulse parameters and the number of applied potential pulses. This method is also faster than the potential scanning method in which only very thin films are obtained.

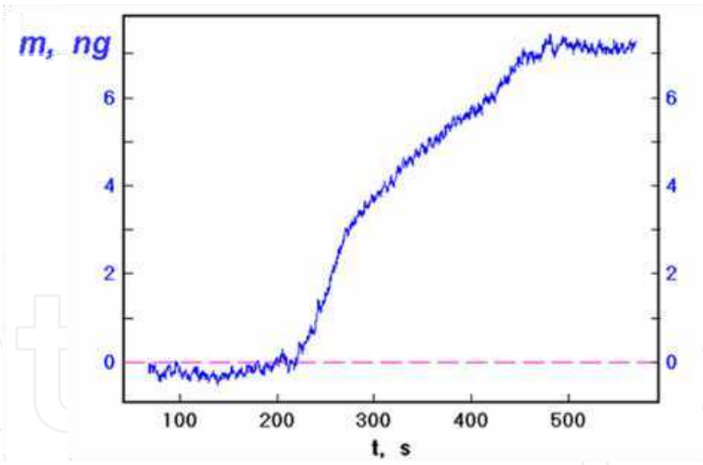

Fig. 10. Apparent mass vs. time response of a GSH-templated poly(oPD) film after injection of a free GSH solution (5 mM).

The process of molecular imprinting of a PoPD(GSH) film synthesized in-situ on a QC/Au/SAM/AuNP substrate is illustrated in Figure 10. The total mass deposited was Δm = 265 ng. After the template removal from the $PoPD_{GSH}$ polymer film, the piezosensor was tested in a solution of 5 mM GSH. Typical time transient recorded upon injection of GSH is presented in Figure 10. The total mass change Δm = 7 ng was observed.
Further improvement of the mass gain can be attained by templating GSH-capped gold nanoparticles in PoPD (Stobiecka et al., 2009). The nanoparticle labeling enhances the

nanogravimetric biosensor response because of the larger mass of the AuNP-labeled analyte.

7. Piezoimmunosensors for glutathione

The analysis of biomarkers of oxidative stress, such as glutathione (GSH), glutathione disulfide (GSSG), 3-nitrotyrosine, homocysteine, nonenal, etc., becomes the key factor for preventive treatments (Knoll et al., 2005, Kohen et al., 2002, Malinski et al., 1992, Reddy et al., 2004 , Stobiecka et al., 2009, Stobiecka et al., 2010a). Since the main redox potential maintaining system in eukaryotic cell homeostasis is the GSH/GSSG redox couple (Noble et al., 2005), we have focused on the design of GSH immunosensor.
The pioneering works in developing immunosensors for GSH have been done by Cliffel and coworkers (Gerdon et al., 2005). They have immobilized the anti-GSH antibody on a protein A layer adsorbed nonspecifically on a gold electrode. The response to GSH-conjugates was monitored by recording the oscillation frequency of the quartz piezoresonator substrate. An extensive review of immunosensors including evaluation of instrumental methods has been published by Skladal et al. (Pohanka et al., 2008, Skládal, 2003).
In this work, the immunosensor design is based on the biorecognition principle with an anti-GSH monoclonal antibody immobilized covalently on a AHT basal SAM through a EDC activated reaction. The anti-GSH Ab molecules were immobilized on a thiol SAM via amide bonds between carboxylic groups of the Fc stem of an Ab and amine groups of the thiol. To control nonspecific binding, the electrodes were incubated with 0.001% BSA solution (Scheme 4).

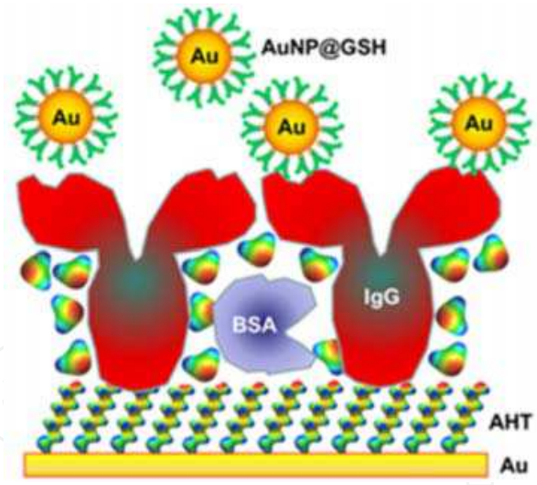

Scheme 4. The design of a nanogravimetric immunosensor for the detection of glutathione-capped AuNP.

The construction of sensory films was carefully monitored by EQCN in each step of the modification of a gold piezoelectrode to confirm binding of molecules and the structure build up on a gold electrode. The resonance frequency response of the AuQC/AHT/Ab_{mono} piezoresonator showed higher affinity towards glutathione-capped gold nanoparticles than to glutathione molecules alone. From the nanogravimetric mass transients, recorded after the injection of 0.95 nM glutathione capped AuNP (Figure 11a), the total resonant frequency shift Δf = 81.45 Hz (Δm = 70.64 ng) was observed. The resonant frequency shift transient, Δf,

for a sensory film AHT/Ab_{mono}, formed on a gold-coated quartz crystal piezoresonator, recorded following an injection of 1.25 mM GSH (final concentration) as the analyte was Δf = 22.99 Hz (Δm = 19.94 ng). The lower immunoreactivity of Ab toward GSH alone indicates that GSH itself does not have the sufficient size to induce the very high affinity with Abmono (Amara et al., 1994). In Figure 11b, the apparent mass change vs. AuNP@GSH concentration is presented. The experimental data were fitted by the least-square fitting routine to give a straight line: $\Delta m = a + b\, C_{AuNP@GSH}$, with intercept a = 2.97 ng, slope b = 63.8 ng/nM (the nanoparticle concentration is given in nM) and the standard deviation σ = 6.74 ng. The limit of detection (LOD) for immunosensor, based on the generalized 3σ method is 0.3 nM.

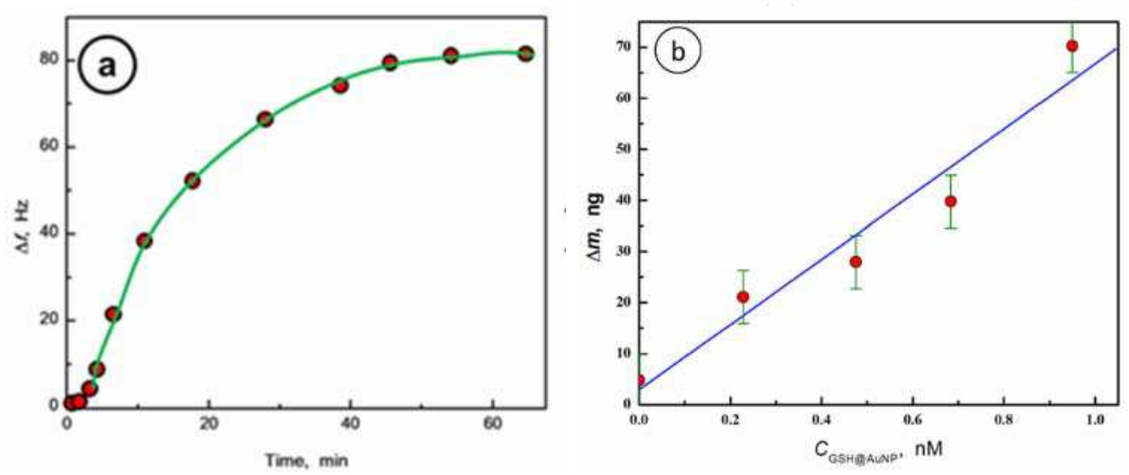

Fig. 11. (a) Resonant frequency transient for a QC/Au/AHT/Ab,BSA piezoimmunosensor recorded after addition of 0.95 nM AuNP@GSH; (b) calibration plot of the apparent mass vs. concentration of AuNP@GSH for a QC/Au/AHT/Ab_{mono} sensor in 50 mM PBS, with surface regeneration in 0.2 M glycine solution, pH = 3, after each test.

8. Label-less redox-probe voltammetric immunosensors

The oxidative stress has been implicated in a wide spectrum of disorders, including cardiovascular and Alzheimer's diseases, accelerates the aging process (Noble et al., 2005), and contributes to the development of autism in children (James et al., 2006). It has also been known that under oxidative stress, serious damage to DNA (formation of 8-oxoguanine, lesions, strand breaks) and to the membrane lipids by overoxidation may occur (Kohen et al., 2002). Therefore, considerable interests in the development of rapid assays for biomarkers of these diseases, such as biological thiols: homocysteine and glutathione have recently surfaced.
We have tested two types of sensors: one with of a positive and one with a negative potential-barrier SAM for the detection of GSH capped AuNP, on the voltammetric signals of ferricyanide $[Fe(CN)6]^{3-}$ redox probes. The anti-GSH antibody molecules were immobilized directly on the short carbon chain thiols (aminohexanethiol or GSH) used for the formation of basal film SAM. The influence of electrostatic interactions in designing sensory films has been well established, including multilayer films with layer-by-layer deposition of oppositely charged polyelectrolytes. In Figure 12, presented are voltammetric characteristics for a ferricyanide redox probe recorded after each step of the sensory film modification.

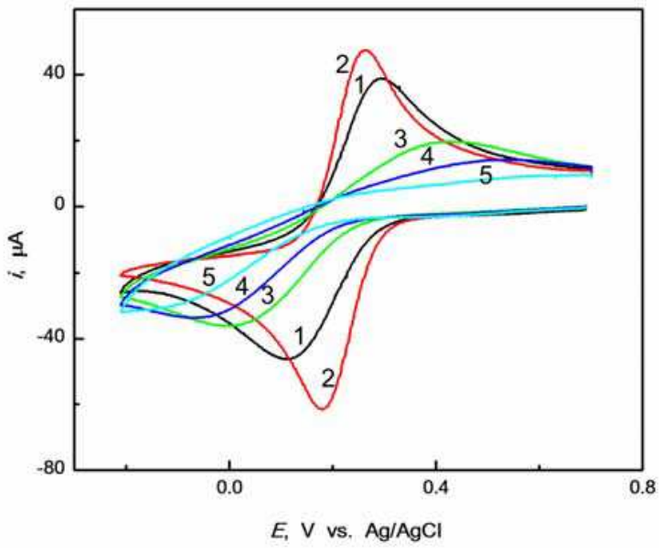

Fig. 12. Cyclic voltammograms for a 1 mM $K_3Fe(CN)_6$ test solution recorded after subsequent steps of the positive potential barrier immunosensor construction: (1) bare gold piezoelectrode and (2-5) gold piezoelectrode after immobilization of successive layers of: (2) 6-amino-1-hexanethiol, (3) monoclonal anti-GSH antibody, (4) bovine serum albumin, (5) glutathione-capped AuNP; v = 100 mV/s.

For a bare gold electrode, a couple of well-developed redox peaks (E_{pc} = 0.111 V and E_{pa} = 0.294 V) was observed (curve 1). The immobilization of AHT on the gold electrode surface results in the increase of the redox marker reaction reversibility (Figure 12, curve 2) since at pH = 7.4 of the test solution, the -NH_2 groups of a AHT film are protonated and attract negatively charged ferricyanide ions. This interaction results in a dramatic decrease of the peak separation of the redox probe, from ΔE = 183 mV for a bare gold electrode, to ΔE = 84 mV for a AuQC/AHT electrode. Thus, the strong electrostatic effect overcomes the thiol-SAM blocking effect leading to the enhancement of the redox probe voltammetric signal. After the immobilization of antibody, the electron transfer of $Fe(CN)_6^{3-/4-}$ couple has been found to decrease due to the formation of a blocking protein layer, reduced surface accessibility, and steric hindrance. Considerable increase of the redox peak separation, from ΔE = 84 mV in the absence of IgG, to ΔE = 408 mV, was observed. The antibody molecules are negatively charged at physiological pH since their isoelectric point (p*I*) is within the interval 4.6-7.2 (Brynda, 2006). Therefore, in addition to the blocking effect, the repulsion of negatively charged redox marker should occur. The GSH recognition process taking place during the incubation of the immunosensor in glutathione-capped AuNP solution leads to the decrease in the redox reaction reversibility of the ferricyanide probe (Figure 12, curve 5). This is consistent with the expected increase of the accumulation of negative charge brought in with GSH-capped AuNP. On the other hand, this behavior contrasts with the expectation of an increased redox activity of a sensor with added metal nanoparticle layer, observed in other systems. The observed effect is then largely dominated by the electrostatic interactions between the probe ions and GSH-capped AuNP bound to the anti-GSH antibody.

The testing of negative potential-barrier immunosensors shows generally weaker responses during the sensory film construction than those observed for positive potential-barrier films (Figure 13).

The GSH-SAM was used as the supporting film for the attachment of an antibody. After forming the GSH-SAM on a gold electrode, the repulsion of $[Fe(CN)_6]^{3-/4-}$ ions from the film was observed and the peak separation in the redox probe voltammetric characteristics increased from ΔE_p = 115 mV for bare gold electrode to ΔE_p = 294 mV for GSH-modified gold electrode. The attachment of an antibody counteracts this behavior and results in an increase of the redox response of the electroactive marker and a decrease in the peak separation for ferricyanide ions to ΔE = 214 mV. The addition of an analyte, GSH-capped AuNP, leads to further increase in the marker signal and a decrease in the peak separation for ferricyanide ions to ΔE = 188 mV. The increase of the ferricyanide probe signal after the immobilization of IgG is expected since a part of the negatively charged GSH-SAM underlayer is covered by IgG which is positively charged on top of the Fab arms thus enhancing the interactions of the sensor with the marker ions. However, the change of the probe signal upon binding the GSH-capped AuNP cannot be explained on the ground of electrostatic interactions since the expected change would be a decrease of the signal due to repulsions between AuNP@GSH and ferricyanide ions, which is not observed. Most likely, the effect of gold nanoparticle addition to the film is playing the dominant role. Therefore, the presence of the interacting conductive Au spheres with coupled surface plasmon oscillations is likely to act as to increase the charge transfer rate of the redox probe ions. The control experiments carried out using sensors without Ab as the recognition layer show no significant changes in the ferricyanide redox probe signal after addition of glutathione-capped gold nanoparticles. They have shown that the glutathione-capped gold nanoparticles can penetrate the blocking BSA film, increasing the conduction pathways and promoting the electron transfer between the redox marker and electrode surface. It is evident that the immobilization of antibody onto the surface of a gold electrode causes a blocking effect and hinders the electron transfer process of the marker ions (Stobiecka et al., 2011).

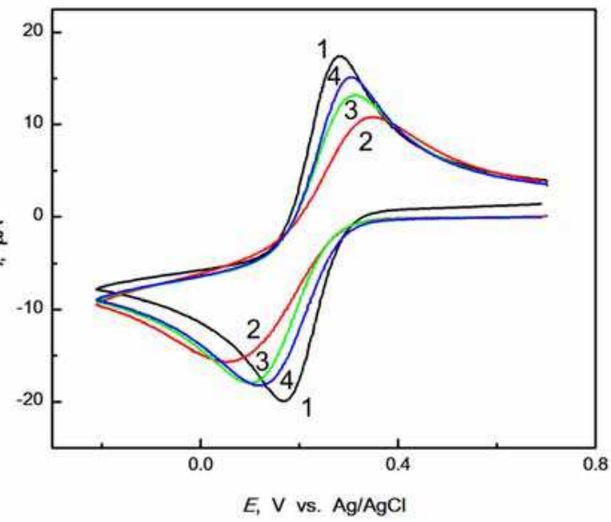

Fig. 13. Cyclic voltammograms of 1 mM $K_3Fe(CN)_6$ in 1 M KNO_3 solution for: (1) bare gold piezoelectrode and (2-4) gold piezoelectrode after immobilization of successive layers: (2) 5 mM glutathione (AuQC/GSH), (3) polyclonal rabbit anti-GSH antibody (AuQC/GSH/Ab_{poly}), (4) glutathione-capped AuNP (AuQC/GSH/Ab_{poly}/AuNP-GSH).

9. Microsensor arrays

Although the accurate advanced instrumental techniques can be used for the analysis of glutathione oxidative stress biomarker (Chiang et al., 2010), there is a need for the development of inexpensive, field-deployable analytical platforms for disease screening and protection against environmental exposure (Noble et al., 2005),(James et al., 2006).

The application of microsensors for screening of biomarkers of oxidative stress has been explored. The responses of sensors operating in the form of a microsensor array have been analyzed by an artificial neural network. The design of microsensor arrays developed in this work is presented in Figure 14. Each of the microsensors consisted of interdigitated electrodes and one reference electrode. The entire chip surface was isolated with the exception of small exposed areas for contact with electrolyte. The sensors were arranged in a group of six sensors in one chip. One of the electrodes of each interdigitated pair was connected to the common and the other had an independent connection. This arrangement enabled measurements of voltammetric characteristics, as well as monitoring of lateral conductance independently in each sensory film with reduced number of interconnections. The experimental setup was configured for the use of a single counter electrode and a single reference electrode reducing the number of electrodes for a six-cell array chip from 18 to 8.

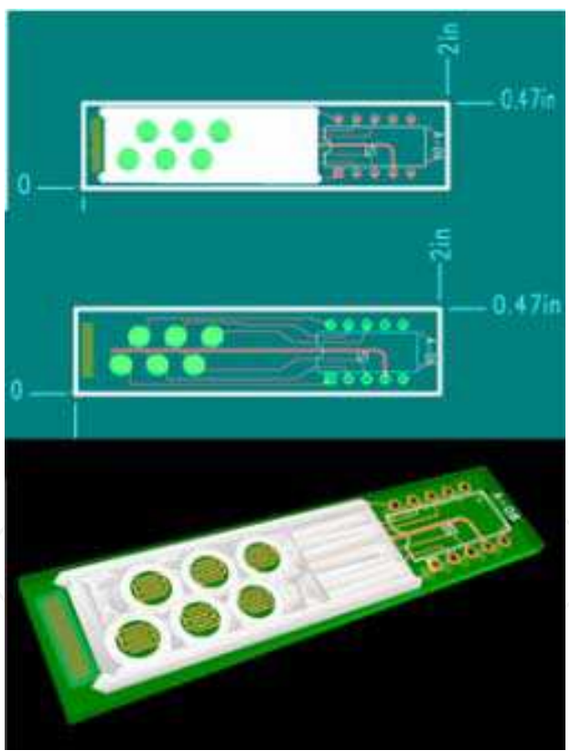

Fig. 14. Design of a microsensor array with pairs of interdigitated electrodes.

In the detection of low level analyte signals superimposed on varying matrix background, the calibration curves have to be constantly adjusted. Also, there are always interfering species which influence the analytical signal. To solve these problems, we have explored the use of artificial neural networks (ANN) that could be designed for a set of input sensors having different responses to the changing matrix, the analyte, and interferences.

The model ANN considered for the analysis of our sensor-array outputs consisted of a basic 4-layer Hopfield neural net presented in Figure 15. The analysis of incoming signals at each node *j* was accomplished using the logistic activation function of the form:

$$g(s_j) = \frac{1}{1 + \exp(-s_j)} \tag{9}$$

where s_j is the sum of inputs to the node *j*:

$$s_j = \sum_{i=1}^{n} w_{ij} y_j + \theta_j \tag{10}$$

where w_{ij} is the weight of the *j*-node connection to the *i*-node in previous layer and θ_j is the bias.

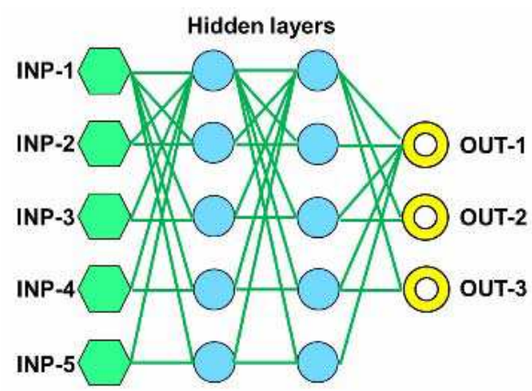

Fig. 15. Scheme of a neural network with input nodes, two hidden layers and an output layer; complete set of connections shown only for the first row of nodes for clarity.

The network was trained using Hopfield backpropagation routines. The artificial neural network approach enables adjusting the network responses to different types of samples, with different background matrix and interferences.
In future developments, the use of microsensor arrays and microfluids will help designing robust and inexpensive point-of-care deployable sensor arrays for oxidative stress biomarkers monitoring.

10. Conclusions

We have demonstrated that RELS and UV-Vis spectroscopy can provide a wealth of information about the interactions of biomarkers of the oxidative stress with gold nanoparticles (AuNP) and can be applied to monitor the ligand-exchange processes followed by AuNP assembly. The interactions of small biomolecules, such as glutathione, homocysteine, or nitrotyrosine with multifunctional gold nanoparticles are important in view of novel biomedical applications of nanoparticles for diagnostic and therapeutic purposes, as well as for the development of biosensors with metal nanoparticle-enhanced responsiveness. The potential application of AuNP in cancer treatment involves targeted drug delivery and photodynamic therapy (PDT). GSH and Hcys interact strongly with the monolayer-protected gold nanoparticles through the thiolate bonding results in an easy

replacement of a self-assembled protecting monolayer on a core-shell gold nanoparticle with the biomarker SAM. By carefully controlling the solution pH, it is possible to fine-tune the biomarker-induced nanoparticle assembly mediated by interparticle zwitterionic interactions and hydrogen bonding. The fine-tuning of the film composition is achieved by utilizing moderator molecules able to control the composition of the monolayer-shell. This process is based on a new paradigm of the ligand-exchange process through the nucleation and growth of 2D ligand domains. The functionalized gold nanoparticles have also been shown to enhance the design of molecularly-templated conductive polymer films for the detection of GSH. The molecular imprinting technique can be applied in polymer sensor designs based on biorecognition principles with piezoelectric transduction. We have also demonstrated that a buried potential barrier, introduced to an immunoglobulin-based sensory film, results in the improvement of voltammetric signals of a redox ion probe. The tests performed with monoclonal anti-glutathione antibody-based sensors using ferricyanide ion probe have shown stronger sensor response to the layer components for films with buried positive potential barrier than for films with negative barrier.

Novel sensing platforms have been explored for the detection of oxidative stress biomarkers. New microsensor arrays have been developed and tested for possible wide scale use in screening autistic children for GSH depletion which has been found to be associated with some phenotype sensitivity to develop autism. The artificial neural network protocol designed for analysis of microsensor array signals has been employed for the assessment of GSH level testing for synthetic solutions and plasma samples of autistic children.

11. Acknowledgement

This work was supported by the U.S. DoD Research Program "Idea", Grant No. AS-73218.

12. References

Alivisatos, A.P.; Johnsson, K.P.; Peng, X.; Wilson, T.E.; Loweth, C.J.; Bruchez, J.M.P. & Schultz, P.G. (1996). Organization of 'Nanocrystal Molecules' Using DNA." Nature, Vol.382, pp. 609-611.

Almazan, G.; Liu, H.N.; Khorchid, A.; Sundararajan, S.; Martinez-Bermudez, A.K. & Chemtob, S. (2000). Exposure of developing oligodendrocytes to cadmium causes HSP72 induction, free radical generation, reduction in glutathione levels, and cell death. Free Radical Bio Med, Vol.29, pp. 858-869.

Alvarez, M.M.; Khoury, J.T.; Schaaff, T.G.; Shafigullin, M.N.; Vezmar, I. & Whetten, R.L. (1997). Optical absorption spectra of nanocrystal gold molecules. J. Phys. Chem. B, Vol.101, pp. 3706-3712.

Amara, A.; Coussemacq, M. & Geffard, M. (1994). Antibodies to reduced glutathione. Brain Res., Vol.659, pp. 237-242.

Bain, C.D.; Evall, J. & Whitesides, G.M. (1989). Formation of monolayers by the coadsorption of thiols on gold: variation in the head group, tail group, and solvent. J. Am. Chem. Soc., Vol.111, pp. 7155-7164.

Barbas, J.; Ellis, W.R.; Santhanagopalan, V.; Blaszczynski, M. & Winge, D.R. (1992). Conversion in the peptides coating cadmium:sulfide crystallites in *Candida glabrata*. J Inorg Biochem, Vol.48, pp. 95-105.

Beard, K.M.; Shangari, N.; Wu, B. & O'Brien, P.J. (2003). Metabolism, not autoxidation, plays a role in alpha-oxoaldehyde- and reducing sugar-induced erythrocyte GSH depletion: relevance for diabetes mellitus. Mol. Cell. Biochem, Vol.252, pp. 331-338.

Bernard, S.; Enayati, A.; Redwood, L.; Roger, H. & Binstock, T. (2001). Autism: a novel form of mercury poisoning. Med Hypotheses, Vol.56, pp. 462-471.

Boushey, C.J.; Beresford, S.A.A.; Omenn, G.S. & Motulsky, A.G. (1995). A quantitative assessment of plasma homocysteine as a risk factor for vascular disease. Probable benefits of increasing folic acid intake. JAMA, Vol.274, pp. 1049-1057.

Brioude, A.; Jiang, X.C. & Pileni, M.P. (2005). Optical properties of gold nanorods: DDA simulations supported by experiments. J. Phys. Chem. B, Vol.109, pp. 13138-13142.

Brynda, E. (2006). Methods for attachment of antibodies onto optical biosensors, In: Optical Chemical Sensors, F. Baldini, (Eds), 387–401, Springer.

Carlo, M.D. & Loeser, R.F. (2003). Increased oxidative stress with aging reduces chondrocyte survival: correlation with intracellular glutathione levels. Arthritis Rheum, Vol.48, pp. 3419-3430.

Carmel, R. & Jacobsen, D.W. (2001). Homocysteine in Health and Disease, Cambridge, U.K.

Chen, Y.-C.; Brazier, J.J.; Yan, M.; Bargo, P.R. & Prahl, S.A. (2004). Fluorescence-based optical sensor design for molecularly imprinted polymers. Sensor Actuator B, Vol.102, pp. 107-116.

Chen, Y.-C.; Wang, Z.; Yan, M. & Prahl, S.A. (2006). Fluorescence anisotropy studies of molecularly imprinted polymers. Luminescence, Vol.21, pp. 7-14.

Chiang, C.-K.; Lin, Y.-W.; Chen, W.-T. & Chang, H.-T. (2010). Accurate quantitation of glutathione in cell lysates through surface-assisted laser desorption/ionization mass spectrometry using gold nanoparticles. Nanomedicine: Nanotechnology, Biology, and Medicine, Vol.6, pp. 530-537.

Clark-Taylor, T. & Clark-Taylor, B.E. (2004). Is autism a disorder of fatty acid metabolism? Possible dysfunction of mitochondrial β-oxidation by long chain acyl-CoA dehydrogenase Med Hypotheses, Vol.62, pp. 970-975.

Clarkson, T.W. (1992). Mercury: Major Issues in Environmental Health. Environ Health Persp, Vol.100, pp. 31-38.

Dameron, C.T.; Reese, R.N.; Mehra, R.K.; Kortan, A.R.; Carroll, P.J.; Steigerwald, M.L.; Brus, L.E. & Winge, D.R. (1989). Biosynthesis of cadmium sulphide quantum semiconductor crystallites. Nature, Vol.338, pp. 596-597.

Draine, B.T. & Flatau, P.J. (1994). Discrete-dipole approximation for scattering calculations. J. Opt. Soc. Am. A, Vol.11, pp. 1491-1499.

Droge, W. (2002). Free radicals inthe physiologic control of cell function. Physiol. Rev., Vol.82, pp. 47-95.

Elghanian, R.; Storhoff, J.J.; Mucic, R.C.; Letsinger, R.L. & Mirkin, C.A. (1997). Selective colorimetric detection of polynucleotides based on the distance-dependent optical properties of gold nanoparticles. Science, Vol.277, pp. 1078-1081.

Etchegoin, P.G.; Ru, E.C.L. & Meyer, M. (2006). An analytic model for the optical properties of gold. J Chem Phys, Vol.125, pp. 164705-1-164705-3.

Gerdon, A.E.; Wright, D.W. & Cliffel, D.E. (2005). Quartz Crystal Microbalance Detection of Glutathione-Protected Nanoclusters Using Antibody Recognition. Anal. Chem., Vol.77, pp. 304-310.

Gonzales, A.L. & Noguez, C. (2007). Influence of Morphology on the Optical Properties of Metal Nanoparticles. J Comput Theor Nanos, Vol.4, pp. 231-238.

Graham, I.M.; Daly, L.E.; Refsum, H.M.; Robinson, K.; Brattström, L.E.; Ueland, P.M.; Palma-Reis, R.J.; Boers, G.H.J.; Sheahan, R.G.; Israelsson, B.; Uiterwaal, C.S.; Meleady, R.; McMaster, D.; Verhoef, P.; Witteman, J.; Rubba, P.; Bellet, H.; Wautrecht, J.C.; Valk, H.W.d.; Lúis, A.C.S.; Parrot-Roulaud, F.M.; Tan, K.S.; Higgins, I.; Garcon, D.; Medrano, M.J.; Candito, M.; Evans, A.E. & Andria, G. (1997). Plasma homocysteine as a risk factor for vascular disease: the European concerted action project. JAMA, Vol.277, pp. 1775-1781.

Greene, N.T. & Shimizu, K.D. (2005). Colorimetric Molecularly Imprinted Polymer Sensor Array using Dye Displacement. J. Am. Chem. Soc., Vol.127, pp. 5695-5700.

Hepel, M. (1996). Composite polypyrrole films switchable between the anion-and cation-exchanger states. Electrochim. Acta, Vol.41, pp. 63-76.

Hepel, M. (1999). Electrode-Solution Interface Studied with Electrochemical Quartz Crystal Nanobalance In: Interfacial Electrochemistry. Theory, Experiment and Applications, A. Wieckowski, (Eds), 599-630, Marcel Dekker, Inc., New York.

Hepel, M. & Scendo, M. (2002). Kinetics of CuEtX film formation on copper piezoelectrodes. J. Electroanal. Chem., Vol.538-539, pp. 121-132.

Hepel, M. & Tewksbury, E. (2003). Ion-gating phenomena of self-assembling glutathione films on gold piezoelectrodes. J. Electroanal. Chem., Vol.552, pp. 291-305.

Hepel, M.; Kumarihamy, I. & Zhong, C.J. (2006). Nanoporous TiO_2-supported bimetallic catalysts for methanol oxidation in acidic media. Electrochem. Commun., Vol.8, pp. 1439-1444.

Hepel, M.; Dela, I.; Hepel, T.; Luo, J. & Zhong, C.J. (2007). Novel dynamic effects in electrocatalysis of methanol oxidation on supported nanoporous TiO_2 bimetallic nanocatalysts. Electrochim. Acta, Vol.52, pp. 5529-5547.

Hianik, T.; Ostatna, V.; Sonlajtnerova, M. & Grman, I. (2007). Influence of ionic strength, pH and aptamer configuration for binding affinity to thrombin. Bioelectrochem, Vol.70, pp. 127-133.

Hostetler, M.J.; Wingate, J.E.; Zhong, C.J.; Harris, J.E.; Vachet, R.W.; Clark, M.R.; Londono, J.D.; Green, S.J.; Stokes, J.J.; Wignall, G.D.; Glish, J.L.; Porter, M.D.; Evans, N.D. & Murray, R.W. (1998). Alkanethiolate gold cluster molecules with core diameters from 1.5 to 5.2 nm: core and monolayer properties as a function of core size. Langmuir, Vol.14, pp. 17-30.

Hostetler, M.J.; Templeton, A.C. & Murray, R.W. (1999). Dynamics of place-exchange reactions on monolayer-protected gold cluster molecule. Langmuir, Vol.15, pp. 3782-3789.

Inouhe, M. (2005). Phytochelatins. Braz. J. Plant Physiol., Vol.17, pp. 65-78.

Jacobsen, D.W. (2000). Hyperhomocysteinemia and Oxidative Stress : Time for a Reality Check? Arterioscler. Thromb. Vasc. Biol., Vol.20, pp. 1182-1184.

Jain, P.K.; Lee, K.S.; El-Sayed, I.H. & El-Sayed, M.A. (2006). Calculated Absorption and Scattering Properties of Gold Nanoparticles of Different Size, Shape, and Composition: Applications in Biological Imaging and Biomedicine. J. Phys. Chem. B, Vol.110, pp. 7238-7248.

James, S.J.; Melnyk, S.; Jernigan, S.; Cleves, M.A.; Halsted, C.H.; Wong, D.J.; Cutler, P.; Bock, K.; Boris, M.; Bradstreet, J.J.; Baker, S.M. & Gaylor, D.W. (2006). Metabolic endophenotype and related genotypes are associated with oxidative stress in children with autism. Am J Med Genet B Neuropsychiatr Genet., Vol.141B, pp. 947-956.

Javanbakht, M.; Fard, S.E.; Mohammadi, A.; Abdouss, M.; Ganjali, M.R.; Norouzi, P. & Safaraliee, L. (2008). Molecularly imprinted polymer based potentiometric sensor for the determination of hydroxyzine in tablets and biological fluids. Anal. Chim. Acta, Vol.612, pp. 65-74.

Jenkins, A.L.; Yin, R. & Jensen, J.L. (2001). Molecularly imprinted polymer sensors for pesticide and insecticide detection in water. Analyst, Vol.126, pp. 798-802.

Johnson, P.B. & Christy, R.W. (1972). Optical Constants of the Noble Metals. Phys. Rev. B, Vol.6, pp. 4370-4379.

Kamat, P.V. (2002). Photophysical, photochemical and photocatalytic aspects of metal nanoparticles. J. Phys. Chem. B, Vol.106, pp. 7729-7744.

Kariuki, N.N.; Luo, J.; Han, L.; Maye, M.M.; Moussa, L.; Patterson, M.; Lin, Y.; Engelhard, M.H. & Zhong, C.J. (2004). Nanoparticle-structured ligand framework as electrode interfaces. Electroanalysis, Vol.16, pp. 120-126.

Kelly, K.L.; Coronado, E.; Zhao, L.L. & Schatz, G.C. (2003). The Optical Properties of Metal Nanoparticles: The Influence of Size, Shape, and Dielectric Environment. J. Phys. Chem. B, Vol.107, pp. 668-677.

Kikuchi, M.; Tsuru, N. & Shiratori, S. (2006). Recognition of terpenes using molecular imprinted polymer coated quartz crystal microbalance in air phase Sci Technol Adv Mat, Vol.7, pp. 156–161.

Knoll, N.; Ruhe, C.; Veeriah, S.; Sauer, J.; Glei, M.; Gallagher, E.P. & Pool-Zobel, B.L. (2005). Genotoxicity of 4-hydroxy-2-nonenal in human colon tumor cells is associated with cellular levels of glutathione and the modulation of glutathione S-transferase A4 expression by butyrate. Toxicol Sci, Vol.86, pp. 27-35.

Kohen, R. & Nyska, A. (2002). Oxidation of Biological Systems: Oxidative Stress Phenomena, Antioxidants, Redox Reactions, and Methods for Their Quantification. Toxicol Pathol, Vol.30, pp. 620-650.

Kooij, E.S. & Poelsema, B. (2006). Shape and size effects in the optical properties of metallic nanorods. Phys. Chem. Chem. Phys, Vol.8, pp. 3349-3357.

Kriz, D.; Kempe, M. & Mosbach, K. (1996). Introduction of molecularly imprinted polymers as recognition elements in conductometric chemical sensors. Sensor Actuator B, Vol.33, pp. 178-181.

Kugimiya, A. & Takeuchi, T. (1999). Molecularly Imprinted Polymer-Coated Quartz Crystal Microbalance for Detection of Biological Hormone. Electroanalysis, Vol.11, pp. 1158-1160.

Lee, K.S. & El-Sayed, M.A. (2005). Dependence of the Enhanced Optical Scattering Efficiency Relative to That of Absorption for Gold Metal Nanorods on Aspect Ratio, Size, End-Cap Shape, and Medium Refractive Index. J. Phys. Chem. B, Vol.109, pp. 20331-20338.

Lee, K.S. & El-Sayed, M.A. (2006). Gold and Silver Nanoparticles in Sensing and Imaging: Sensitivity of Plasmon Response to Size, Shape, and Metal Composition. J. Phys. Chem. B, Vol.110, pp. 19220-19225.

Lentz, S.R. & Haynes, W.G. (2004). Homocysteine: Is it a clinically important cardiovascular risk factor? Clev Clin J Med, Vol.71, pp. 729-734.

Levit, N.; Pestov, D. & Tepper, G. (2002). High surface area polymer coatings for SAW-based chemical sensor applications. Sensors and Actuators B, Vol.82, pp. 241-249.

Li, F. & Zu, Y. (2004). Effect of Nonionic Fluorosurfactant on the Electrogenerated Chemiluminescence of the Tris(2,2′-bipyridine)ruthenium(II)/Tri-n-propylamine

System: Lower Oxidation Potential and Higher Emission Intensity. Anal. Chem., Vol.76, pp. 1768-1772.

Liang, C.; Peng, H.; Nie, L. & Yao, S. (2000). Bulk acoustic wave sensor for herbicide assay based on molecularly imprinted polymer Fresenius' J. Anal. Chem, Vol.367, pp. 551-555.

Lim, I.I.S.; Ip, W.; Crew, E.; Njoki, P.N.; Mott, D.; Zhong, C.J.; Pan, Y. & Zhou, S. (2007). Homocysteine-mediated reactivity and assembly of gold nanoparticles. Langmuir, Vol.23, pp. 826-833.

Lim, I.I.S.; Mott, D.; Ip, W.; Njoki, P.N.; Pan, Y.; Zhou, S. & Zhong, C.J. (2008). Interparticle interactions of glutathione mediated assembly of gold nanoparticles. Langmuir, Vol.24, pp. 8857-8863.

Lim, S.I. & Zhong, C.J. (2009). Molelucarly Mediated Processing and Assembly of Nanoparticles: Exploring the Interparticle Interactions and Structures. Accounts of chemical research, Vol.42, pp. 798-808.

Link, S. & El-Sayed, M.A. (1999a). Spectral properties and relaxation dynamics of surface plasmon electronic oscillations in gold and silver nanodots and nanorods. J. Phys. Chem. B, Vol.103, pp. 8410-8426.

Link, S.; Mohamed, M.B. & El-Sayed, M.A. (1999b). Simulation of the Optical Absorption Spectra of Gold Nanorods as a Function of Their Aspect Ratio and the Effect of the Medium Dielectric Constant. J. Phys. Chem. B, Vol.103, pp. 3073-3077.

Mahony, J.O.; Nolan, K.; Smyth, M.R. & Mizaikoff, B. (2005). Molecularly imprinted polymers—potential and challenges in analytical chemistry. Anal Chim Acta, Vol.534, pp. 31-39.

Malinski, T. & Taha, Z. (1992). Nitric oxide release from a single cell measured in situ by a porphyrinic-based microsensor. Nature, Vol.358, pp. 676-678.

Malitesta, C.; Picca, R.A.; Ciccarella, G.; Sgobba, V. & Brattoli, M. (2006). Synthesis of a Molecularly Imprinted Polymer for Dioxin. Sensors, Vol.6, pp. 915-924.

Masque, N.; Marce, R.M. & Borrull, F. (2001). Molecularly imprinted polymers: new tailor-made materials for selective solid-phase extraction. Trends Anal. Chem, Vol.20, pp. 477-486.

Matsuguchi, M. & Uno, T. (2006). Molecular imprinting strategy for solvent molecules and its application for QCM-based VOC vapor sensing. Sensor Actuator B, Vol.113, pp. 94-99.

Maye, M.M.; Lim, I.I.S.; Luo, J.; Rab, Z.; Rabinovich, D.; Liu, T. & Zhong, C.J. (2005). Mediator-Template Assembly of Nanoparticles. J. Am. Chem. Soc., Vol.127, pp. 1519-1529.

Mehra, R.K. & Winge, D.R. (1991). Metal ion resistance in fungi: molecular mechanisms and their regulated expression. J. Cell. Biochem., Vol.45, pp. 30-40.

Mills, J.L.; Scott, J.M.; Kirke, P.N.; McPartlin, J.M.; Conley, M.R.; Weir, D.G.; Molloy, A.M. & Lee, Y.J. (1996). Homocysteine and neural tube defects. J Nutr, Vol.126, pp. 756S-760S.

Mishchenko, M.; Travis, L.D. & Lacis, A.A. (2002). Scattering, Absorption, and Emission of Light by Small Particles, Cambridge.

Moreno-Bondi, M.C.; Benito-Pena, E.; San-Vicente, B.; Navarro-Villoslada, F.; Leon, M.E.d.; Orellana, G.; Aparicio, S.; Molina, J.; Kempe, M. & Fiaccabrino, G.C. (2003). Molecularly imprinted polymers as selective recognition elements for optical

sensors based on fluorescent measurements. Digest of Technical Papers. Transducers '03 Boston, 12th International Conference on Solid-State Sensors, Actuators and Microsystems Vol.2, pp. 975-978.

Noble, M.; Mayer-Proschel, M. & Proschel, C. (2005). Redox Regulation of Precursor Cell Function: Insights and Paradoxes. Antioxid Redox Sign, Vol. 7, pp. 1456-1467

Panasyuk, T.L.; Mirsky, V.M.; Piletsky, S.A. & Wolfbeis, O.S. (1999). Electropolymerized Molecularly Imprinted Polymers as Receptor Layers in Capacitive Chemical Sensors. Anal. Chem., Vol.71, pp. 4609-4613.

Park, S.J.; Taton, T.A. & Mirkin, C.A. (2002). Array-based electrical detection of DNA with nanoparticle probe. Science, Vol.295, pp. 1503-1506

Percival, C.J.; Stanley, S.; Galle, N.; Braihwaite, A.; Newton, M.I.; McHale, G. & Hayes, W. (2001). Molecular-Imprinted, Polymer-Coated Quartz Crystal Microbalances for the Detection of Terpenes. Anal. Chem., Vol.73, pp. 4225-4228.

Perez-Juste, J.; Pastoriza-Santos, I.; Liz-Marzan, L.M. & Mulvaney, P. (2005). Gold nanorods: Synthesis, characterization and applications. Coordin Chem Rev, Vol.249, pp. 1870–1901.

Perez, N.; Whitcombe, M.J. & Vulfson, E.N. (2000). Molecularly imprinted nanoparticles prepared by core-shell emulsion polymerization. J. App. Polym. Sci, Vol.77, pp. 1851-1859.

Piletsky, S.A.; Subrahmanyam, S. & Turner, A.P.F. (2001). Application of molecularly imprinted polymers in sensors for the environment and biotechnology. Sensor Rev, Vol.21, pp. 292 - 296.

Ping, Y.; Hanson, D.; Koslow, I.; Ogitsu, T.; Prendergast, O.; Schwegler, E.; Collins, G. & Ng, A. (2008). Dielectric function of warm dense gold. Phys. Plasmas, Vol.15, pp. 56303-056303-7.

Pohanka, M. & Skládal, P. (2008). Electrochemical biosensors – principles and applications. J. Appl. Biomed., Vol.6, pp. 57-64.

Polidoro, G.; Ilio, C.D.; Arduini, A.; Rovere, G.L. & Federici, G. (1984). Superoxide dismutase, reduced glutathione and TBA-reactive products in erythrocytes of patients with multiple sclerosis. Int. J. Biochem, Vol.16, pp. 505-509.

Prasad, B.B. & Lakshmi, D. (2005). Barbituric Acid Sensor Based on Molecularly Imprinted Polymer- Modified Hanging Mercury Drop Electrode. Electroanalysis, Vol.17, pp. 1260-1268.

Prescott, S.W. & Mulvaney, P. (2006). Gold nanorod extinction spectra. J. Appl. Phys. , Vol.99, pp. 123504.

Priego-Capote, F.; L.Ye; Shakil, S.; Shamsi, S.A. & Nilsson, S. (2008). Monoclonal Behavior of Molecularly Imprinted Polymer Nanoparticles in Capillary Electrochromatography. Anal. Chem., Vol.80, pp. 2881-2887.

Reddy, S. & Bradley, J. (2004). Immunohistochemical Demonstration of Nitrotyrosine, a Biomarker of Oxidative Stress, in Islet Cells of the NOD Mouse. Ann. N. Y. Acad. Sci., Vol.1037, pp. 199-202.

Refsum, H.; Ueland, P.M.; Nygard, O. & Vollset, S.E. (1989). Homocysteine and cardiovascular disease. Annu Rev Med, Vol.49, pp. 31-62.

Repetto, M.; Reides, C.; Carretero, M.L.G.; Costa, M.; Griemberg, G. & Llesuy, S. (1996). Oxidative stress in blood of HIV infected patients. Clin. Chim. Acta, Vol.255, pp. 107-117.

Reynolds, R.A.; Mirkin, C.A. & Letsinger, R.L. (2000). Homogeneous, nanoparticle-based quantitative colorimetric detection of oligonucleotides. J. Am. Chem. Soc., Vol.122, pp. 3795-3796.

Sergeyeva, T.A.; Piletsky, S.A.; Panasyuk, T.L.; El'skaya, A.V.; Brovko, A.A.; Slinchenko, E.A. & Sergeeva, L.M. (1999). Conductimetric sensor for atrazine detection based on molecularly imprinted polymer membranes. Analyst, Vol.124, pp. 331-334.

Seshadri, S.; Beiser, A.; Selhub, J.; Jaques, P.F.; Rosenberg, I.H.; D'Agostino, R.B.; Wilson, P.W. & Wolf, P.A. (2002). Plasma homocysteine as a risk factor for dementia and Alzheimer's disease. NEJM, Vol.346, pp. 476-483.

Sestrem, R.H.; Ferreira, D.C.; Landers, R.; Temperini, M.L.A. & Nascimento, G.M.d. (2010). Synthesis and spectroscopic characterization of polymer and oligomers of ortho-phenylenediamine. Eur Polym J, Vol.46, pp. 484-493.

Skládal, P. (2003). Piezoelectric quartz crystal sensors applied for bioanalytical assays and characterization of affinity interactions. J. Brazil. Chem. Soc., Vol.14, pp. 491-502.

Stephenson, C.J. & Shimizu, K.D. (2007). Colorimetric and fluorometric molecularly imprinted polymer sensors and binding assays. Polym Int, Vol.56, pp. 482-488.

Stobiecka, M.; Deeb, J. & Hepel, M. (2009). Molecularly Templated Polymer Matrix Films for Biorecognition Processes: Sensors for Evaluating Oxidative Stress and Redox Buffering Capacity. ECS Transactions, Vol.19, pp. 15-32.

Stobiecka, M.; Coopersmith, K. & Hepel, M. (2010a). Resonance elastic light scattering (RELS) spectroscopy of fast non-Langmuirian ligand-exchange in glutathione-induced gold nanoparticle assembly. J. Coll. Interf. Sci., Vol.350, pp. 168-177.

Stobiecka, M.; Deeb, J. & Hepel, M. (2010b). Ligand exchange effects in gold nanoparticle assembly induced by oxidative stress biomarkers: Homocysteine and cysteine. Biophys Chem, Vol.146, pp. 98-107.

Stobiecka, M. & Hepel, M. (2011). Effect of buried potential barrier in label-less electrochemical immunodetection of glutathione and glutathione-capped gold nanoparticles. Biosens. Bioelectron., Vol.26, pp. 3524-3530.

Storhoff, J.J.; Elghanian, R.; Mucic, R.C.; Mirkin, C.A. & Letsinger, R.L. (1998). One-pot colorimetric differentiation of polynucleotides with single base imperfections using gold nanoparticle probes. J. Am. Chem. Soc., Vol.120, pp. 1959-1964.

Taton, T.A.; Mucic, R.C.; Mirkin, C.A. & Letsinger, R.L. (2000). The DNA-mediated formation of supramolecular mono- and multilayered nanoparticle structures. J. Am. Chem. Soc., Vol.122, pp. 6305-6306.

Taton, T.A.; Lu, G. & Mirkin, C.A. (2001). Two-color labeling of oligonucleotide arrays via size-selective scattering of nanoparticle probes. J. Am. Chem. Soc., Vol.123, pp. 5164-5165.

Tokareva, I.; Tokarev, I.; Minko, S.; Hutter, E. & Fendle, J.H. (2006). Ultrathin molecularly imprinted polymer sensors employing enhanced transmission surface plasmon resonance spectroscopy. Chem. Commun., pp. 3343-3345

Tombelli, S.; Minunni, M.; Luzi, E. & Mascini, M. (2005). Aptamer-based biosensors for the detection of HIV-1 Tat protein. Bioelectrochemistry Vol.67, pp. 135- 141.

Tsuru, N.; Kikuchi, M.; Kawaguchi, H. & Shiratori, S. (2006). A quartz crystal microbalance sensor coated with MIP for ''Bisphenol A'' and its properties. Thin Solid Films, Vol.499, pp. 380-385.

Ungureanu, C.; Rayavarapu, R.G.; Manohar, S. & Leeuwen, T.G.v. (2009). Discrete dipole approximation simulations of gold nanorod optical properties: Choice of input

parameters and comparison with experiment. J. App. Phys., Vol.105, pp. 102032-102032-7.

Upadhya, S.; Upadhya, S.; Mohan, S.K.; Vanajakshamma, K.; Kunder, M. & Mathias, S. (2004). Oxidant-antioxidant status in colorectal cancer patients before and after treatment. Indian J Clin Biochem, Vol.19 pp. 80-83.

Varadarajan, S.; Kanski, J.; Aksenova, M.; Lauderback, C. & Butterfield, D.A. (2001). Different mechanisms of oxidative stress and neurotoxicity for Alzheimer's A*b*(1-42) and A*b*(25-35). J. Am. Chem. Soc., Vol.123, pp. 5625-5631.

Vatamaniuk, O.K.; Mari, S.; Lu, Y.P. & Rea, P.A. (2000). Mechanism of Heavy Metal Ion Activation of Phytochelatin (PC) Synthase.Blocked thiols are sufficient for PC synthase-catalyzed transpeptidation of glutathione and related thiol peptides. J Biol Chem, Vol.275, pp. 31451-31459.

Vatamaniuk, O.K.; Bucher, E.A.; Ward, J.T. & Rea, P.A. (2001). A New Pathway for Heavy Metal Detoxification in Animals. Phytochelatin synthase is required for cadmium tolerance in *Caenorhabditis elegans.* J Biol Chem, Vol.276, pp. 20817-20820.

Welch, G.N. & Loscalzo, J. (1998). Homocysteine and atherothrombosis. NEJM, Vol.338, pp. 1042-1050.

Whitesides, G.M.; Kriebel, J.K. & Love, J.C. (2005). Molecular Engineering of Surfaces using Self-Assembled Monolayers. Sci Prog, Vol.88, pp. 17-48.

Yamamoto, Y. & Yamashita, S. (2002). Ubiquinol/ubiquinone ratio as a marker of oxidative stress, In: Methods in Molecular Biology. Oxidative Stress Biomarkers and Antioxidant Protocols, D. Armstrong, (Eds), 241-246, Totowa, NJ.

Yan, M. & Ramstrom, O. (2005). Molecularly Imprinted Materials. Science and Technology, New York.

Yang, W.H.; Schatz, G.C. & Duyne, R.P.V. (1995). Discrete dipole approximation for calculating extinction and Raman intensities for small particles with arbitrary shapes. J Chem Phys, Vol.103, pp. 869-875.

Ye, L.; Weiss, R. & Mosbach, K. (2000). Synthesis and Characterization of Molecularly Imprinted Microspheres. Macromolecules, Vol.33, pp. 8239-8245.

Yilmaz, E.; Mosbach, K. & Haupt, K. (1999). Influence of functional and cross-linking monomers and the amount of template on the performance of molecularly imprinted polymers in binding assays. Anal. Commun., Vol.36, pp. 167-170.

Yin, G.; Wang, S.Y.; Xu, M. & Chen, L.Y. (2006). Theoretical Calculation of the Optical Properties of Gold Nanoparticles. J Korean Phys Soc, Vol.49, pp. 2108-2111.

Zhang, X.; Li, H.; Jin, H.; Ebin, Z.; Brodsky, S. & Goligorsky, M.S. (2000). Effects of homocysteine on endothelialnitric nitric oxide production. Am. J. Physiol. Renal. Physiol., Vol.279, pp. F671-F678.

Zheng, W.; Maye, M.M.; Leibowitz, F.L. & Zhong, C.J. (2000). Imparting Biomimetic Ion-Gating Recognition Properties to Electrodes with a Hydrogen-Bonding Structured Core-Shell Nanoparticle Network. Anal. Chem., Vol.72, pp. 2190-2199.

New Perspectives in Biosensors Technology and Applications
Edited by Prof. Pier Andrea Serra

ISBN 978-953-307-448-1
Hard cover, 448 pages
Publisher InTech
Published online 27, July, 2011
Published in print edition July, 2011

A biosensor is a detecting device that combines a transducer with a biologically sensitive and selective component. Biosensors can measure compounds present in the environment, chemical processes, food and human body at low cost if compared with traditional analytical techniques. This book covers a wide range of aspects and issues related to biosensor technology, bringing together researchers from 12 different countries. The book consists of 20 chapters written by 69 authors and divided in three sections: Biosensors Technology and Materials, Biosensors for Health and Biosensors for Environment and Biosecurity.

INTECH
open science | open minds

InTech Europe
University Campus STeP Ri
Slavka Krautzeka 83/A
51000 Rijeka, Croatia
Phone: +385 (51) 770 447
Fax: +385 (51) 686 166
www.intechopen.com

InTech China
Unit 405, Office Block, Hotel Equatorial Shanghai
No.65, Yan An Road (West), Shanghai, 200040, China
中国上海市延安西路65号上海国际贵都大饭店办公楼405单元
Phone: +86-21-62489820
Fax: +86-21-62489821

IntechOpen